A Single-Cell Molecular Atlas of White Adipose Tissue Shows Differences in Myeloid and Lymphoid Cell Polarization in Type 2 Diabetes and HIV Infection

Authors: Samuel S. Bailin[1], Jonathan A. Kropski[2,3,4], Rama D. Gangula[5], LaToya Hannah[6], Joshua D. Simmons[5], Mona Mashayekhi[6], Fei Ye[7], Run Fan[7], Abha Chopra[8], Ramesh Ram[8], Simon Mallal[1,5,8-10], Christian M. Warren[5], Spyros A. Kalams[1,5,10], Curtis L. Gabriel[11], Celestine N. Wanjalla[1,10,±*], John R. Koethe[1,3,10,±]

[1]Department of Medicine, Division of Infectious Diseases, Vanderbilt University Medical Center, Nashville, Tennessee, USA
[2]Department of Medicine, Division of Allergy and Pulmonology, Vanderbilt University Medical Center, Nashville, Tennessee, USA
[3]Veterans Affairs Tennessee Valley Healthcare System, Nashville, Tennessee, USA
[4]Deparment of Cell and Developmental Biology, Vanderbilt University, Nashville, Tennessee, USA
[5]Tennessee Center for AIDS Research, Vanderbilt University Medical Center, Nashville, Tennessee, USA
[6]Department of Medicine, Division of Diabetes, Endocrinology, and Metabolism, Vanderbilt University Medical Center, Nashville, Tennessee, USA
[7]Department of Biostatics, Vanderbilt University, Nashville, Tennessee, USA
[8]Insitute for Immunology and Infectious Diseases, Murdoch University, Perth, WA, Australia
[9]Vanderbilt Technologies for Advanced Genomics, Vanderbilt University Medical Center, Nashville, Tennessee, USA
[10]Center for Translational Immunology and Infectious Diseases, Vanderbilt University Medical Center, Nashville, Tennessee, USA
[11]Department of Medicine, Division of Gastroenterology, Hepatology, and Nutrition, Nashville, Tennessee, USA

[*]Corresponding Author: Celestine N. Wanjalla, MD, Ph.D.; Division of Infectious Diseases, Vanderbilt University Medical Center, A-2200 MCN, 1161 21st Avenue South, Nashville, Tennessee, 37232-2582. (615) 322-2035 (o), (615) 343-6160 (f), celestine.wanjalla@vumc.org

[±]These authors contributed equally

Running Title: Adipose tissue in HIV and Diabetes

Abstract

Subcutaneous white adipose tissue (scWAT) is a critical regulator of systemic metabolic homeostasis. HIV infection is accompanied by alterations in scWAT immune cells, which may contribute to the increased risk for cardiometabolic diseases in persons with HIV (PWH) and serve as a model to investigate cellular relationships. We generated the largest molecular atlas of scWAT in humans to date from 91 individuals using paired single-cell transcriptomic and proteogenomics to determine the scWAT immune profile in non-diabetic, pre-diabetic, and diabetic PWH, and HIV-negative diabetic persons. We identified a substantial increase in lipid-associated macrophages (LAMs) with glucose intolerance, and, in PWH only, $CD4^+$ and $CD8^+$ T effector memory cells were correlated with LAM proportion. Finally, we resolved adipogenic and fibrogenic cells at high resolution and found a strong association between LAMs and myofibroblasts. These results provide a high-resolution, multi-platform characterization of changes in scWAT composition that occur with metabolic disease and HIV.

Keywords: human immunodeficiency virus, type 2 diabetes mellitus, white adipose tissue, subcutaneous adipose tissue, single-cell RNA sequencing, immune cells

Introduction

The rising global rates of obesity and type 2 diabetes mellitus represent a significant public health challenge (Jaacks et al., 2019; Saeedi et al., 2019). Adipose tissue is an important regulator of glucose and lipid metabolism, and alterations in its cellular composition and function have been implicated in the development of metabolic disease (Ghaben and Scherer, 2019). Chronic adipose tissue inflammation is a hallmark of obesity and is regulated by multiple immune cells, including macrophages (Hill et al., 2018; Jaitin et al., 2019; Kratz et al., 2014), $CD8^+$ T cells (Nishimura et al., 2009), $CD4^+$ T cells (Feuerer et al., 2009), innate lymphoid cells (ILCs) (Boulenouar et al., 2017; Brestoff et al., 2015), γδ T cells (Goldberg et al., 2020; Kohlgruber et al., 2018), and natural killer cells (NK) (Lee et al., 2016). Adipose tissue immune cell-derived inflammatory cytokines alter adipocyte metabolism and interfere with insulin-signaling and lipid storage (Lumeng et al., 2007b). Therefore, defining the interactions between subcutaneous white adipose tissue (scWAT) immune cells and components of adipose tissue is critical for identifying changes that may contribute to metabolic diseases.

Persons with HIV (PWH) can survive decades on modern antiretroviral therapy (ART), but this success is offset by an increasing burden of metabolic disease (Herrin et al., 2016; Nansseu et al., 2018; Shah et al., 2018). Despite effective suppression of plasma viremia with ART, PWH have persistent innate and adaptive immune activation (Neuhaus et al., 2010; Zicari et al., 2019), and changes in the adipose tissue immune cell compartment (Couturier et al., 2015; Damouche et al., 2015; Wanjalla et al., 2019). In non-obese PWH, $CD8^+$ T cells accumulate in scWAT in a process that is strikingly similar to that observed in obesity in the general population (Couturier et al., 2015; Nishimura et al., 2009; Wanjalla et al., 2019). Additionally, scWAT $CD4^+$ T cells also differ in PWH versus HIV-negative individuals, which is irrespective of

obesity. In PWH, $CD4^+$ T cells expressing the surface markers CX3CR1, GPR56, and CD57 (C-G-C^+) that are predominately T effector memory (T_{EM}) and T effector memory RA (T_{EMRA}) phenotype accumulate in scWAT with progressive glucose intolerance. In contrast, a separate population of $CD4^+$ T cells expressing CD69, a marker of tissue residence, (Sathaliyawala et al., 2013) predominate in scWAT of HIV-negative persons (Wanjalla et al., 2019; Wanjalla et al., 2021). Despite the importance of scWAT to metabolic health, a comprehensive assessment of the identity, polarization, and molecular programs of adipose tissue immune cells in PWH, a group at increased risk of metabolic disease, and HIV-negative individuals with glucose intolerance has not been reported. Investigating the unique and shared features of scWAT in the context of HIV and diabetes may provide further insight into the role of T cells and other immune cells in the pathogenesis of glucose intolerance.

Several studies have used single-cell RNA sequencing (scRNA-seq) to characterize the cellular composition in the adipose tissue compartment in mice and humans, primarily in the context of obesity research (Acosta et al., 2017; Emont et al., 2022; Hildreth et al., 2021; Merrick et al., 2019; Sarvari et al., 2021; Vijay et al., 2020). However, there are currently few data on the cellular composition of adipose tissue in the context of metabolic disease and diabetes, particularly among groups at elevated risk such as PWH. To address this research gap, we recruited a large cohort of PWH with a spectrum of metabolic health from normal to diabetic, in addition to HIV-negative persons with diabetes, to define the adipose tissue immune cell profiles accompanying HIV infection and diabetes. Using single-cell proteogenomics, we generated a detailed molecular atlas of scWAT from 91 individuals and characterized disease-specific changes in cellular populations and expression programs. We found a dramatic increase of lipid-associated macrophages (LAMs) with glucose intolerance that was independent of body mass

index (BMI) and HIV serostatus. In contrast, an increase in the $CD4^+$ and $CD8^+$ T effector memory cell population was associated with glucose intolerance and correlated with LAM proportion in PWH only, potentially reflecting an enhanced or differential role of T cells in the development of metabolic disease among PWH. Finally, we observed diversity in adipogenic cells not previously characterized in humans, including a strong association between LAMs and myofibroblasts independent of glucose intolerance and BMI. Our comprehensive molecular atlas of scWAT is the largest to date, includes disease states not previously characterized, and advances understanding of how complex interactions between diverse immune and stromal cells contribute to metabolic dysregulation.

Results

Single-Cell Proteogenomic Profiling of Subcutaneous White Adipose Tissue Reveals Heterogeneity of Cell Populations by Disease State

To determine the cell populations that characterize scWAT in the context of diabetes and HIV infection, we collected abdominal scWAT from non-diabetic PWH (n = 20), pre-diabetic PWH (n = 19), diabetic PWH (n = 20), and HIV-negative diabetic persons (n = 32). We used Cellular Indexing of Transcriptomes and Epitopes by Sequencing (CITE-seq)(Stoeckius et al., 2017) coupled with 10x scRNA-seq to analyze surface phenotypes and transcriptomes (**Figures 1A**, **S1A**, STAR methods). Participants were enrolled in a clinical cohort to investigate the role of adipose tissue immune cells in the development of metabolic disease among persons with and without HIV registered at ClinicalTrials.gov (NCT04451980) (**Table 1**). After quality control filtering (**Figures S1B-E**) and harmony batch correction (Korsunsky et al., 2019), we obtained a final dataset including 283,491 cells from 91 participants (**Figures 1B, 1C, and S1E**). We

identified 48 major cell types/states using genes previously identified in single-cell datasets (Angueira et al., 2021; Brown et al., 2019; Dutertre et al., 2019; Hao et al., 2021; Hildreth et al., 2021; Hu et al., 2021; Jaitin et al., 2019; Merrick et al., 2019; Muhl et al., 2020; Schupp et al., 2021; Travaglini et al., 2020; Vijay et al., 2020) (**S1F; Tables S1 and S2**). Broadly, cells clustered into stromal (n = 87,674 cells; *COL1A2, CCDC80*), lymphoid (n = 33,733 cells; *CD3E, NKG7, MS4A1, MZB1*), vascular (n = 93,453 cells; *CLDN5, ACTA2, PECAM1*), and myeloid cells (n = 68,631 cells; *LYZ, CD14, CD68, CD1C*) (**Figure 1D)**. Importantly, we identified several immune cell types that have been associated with diabetes and obesity in prior studies, including lipid-associated macrophages, NK cells, γδ T cells, and ILCs (some cell types were aggregated for visualization). We also identified three clusters (aterial-EndoMT-like, venous-EndoMT-like, capillary-EndoMT-like) expressing markers of both pericytes and endothelial cells. Pseudotime analysis shows progressive loss of endothelial cell markers and acquisition of pericyte markers (**Figures S1G and S1H**), and upregulation of the transcription factor SNAI1, which has been associated with endothelial-mesenchymal transition (Piera-Velazquez and Jimenez, 2019).

HIV-negative participants with diabetes had significantly fewer lymphoid cells as a percentage of total cells compared with diabetic PWH (median percent lymphoid 5.1% vs. 15.1%, respectively; p = 0.004), but there was no difference in the percentage of myeloid cells (median percent myeloid 23.5% vs. 23.7% respectively; p = 0.52; **Figure 1E**). These findings are consistent with previous studies that found T cell enrichment in scWAT of PWH irrespective of metabolic disease (Couturier et al., 2015). Comparing non-diabetic, prediabetic and diabetic PWH, myeloid (median percent: 34.1%, 19.3%, 23.7%, respectively; p = 0.23) and lymphoid (median percent: 24.7%, 8.8%, 15.1%, respectively; p = 0.17) proportions were not significantly

different (**Figure 1E**). Age and sex can influence adipocyte function and immune cell populations (Caso et al., 2013; Chang et al., 2018; Huang et al., 2021; Vasanthakumar et al., 2020), but we found no significant differences in cell proportions after stratifying by these factors. Taken together, these data represent the largest single-cell genomic, and first proteogenomic, comprehensive atlas of scWAT, as well as the first characterization of scWAT in persons with diabetes and HIV infection.

Lipid-Associated Macrophages Accumulate with Glucose Intolerance

Adipose tissue macrophages and conventional dendritic cells (cDCs) interact closely with adipocytes. These antigen-presenting cells modulate adipogenesis, insulin sensitivity, and tissue remodeling and undergo dramatic functional changes in the setting of obesity (Amano et al., 2014; Cinti et al., 2005; Hill et al., 2018; Jaitin et al., 2019; Lumeng et al., 2007a; Macdougall et al., 2018; Russo and Lumeng, 2018). Similar data are limited in HIV infection, but studies of PWH with lipodystrophy suggest an increase in adipose tissue macrophage inflammatory mediators compared with HIV-negative individuals (Jan et al., 2004; Shikuma et al., 2014).

To evaluate the myeloid compartment, we clustered on 68,631myeloid cells and identified 12 distinct cell populations (**Figures 2A and S2A**) using canonical gene markers (**Figures 2B and S2B; Table S3**). Surface-marker phenotyping by CITE-seq supported our classification of LAMs ($CD11C^{+}$), perivascular macrophages (PVMs) ($CD11C^{-}$), non-classical monocytes ($CD16^{+}$), classical monocytes ($CD14^{+}$), and dendritic cells ($CD1C^{+}$) (**Figure S2C**). We identified LAMs based on the expression of *CD9* and *TREM2* that are important for lipid scavenging and removing apoptotic cells (**Figure 2C**) (Hill et al., 2018; Jaitin et al., 2019). PVMs are resident tissue macrophages that express *LYVE1*, *RNASE1* (Chakarov et al., 2019),

and are important for maintaining metabolic homeostasis in healthy individuals (Russo and Lumeng, 2018). A third macrophage cluster that we categorized as monocyte-macrophages had high expression of *HLA* genes, *CXCL2, CXCL3,* and monocyte markers. A final cluster expressed metallothionein genes and genes regulating inflammation (*MIF, ISG15, C15orf48*). Gene Ontology over-representation analysis using the top genes for each macrophage cluster showed distinct enrichment of lipid processing genes in LAMs, myeloid recruitment genes in PVMs, viral responses and translation genes in monocyte-macrophages, and antigen presentation genes in other macrophages, confirming that gene expression patterns correspond to specific biological roles in adipose tissue (**Figure 2D**).

Recent studies using scRNA-seq have demonstrated the heterogeneity of dendritic cells and identified cDC2A and *AXL*$^{+}$ dendritic cells (Brown et al., 2019; Dutertre et al., 2019). We found cDC1 (*CLEC9A*, *XCR1*), cDC2B (*CD1C, FCER1A*), and CCR7^{hi} DC or mature regulatory DC (*CCR7, LAMP3, CD1C*) but we did not identify cDC2A or AXL^{+} DCs in scWAT. The proportion of cDC1 was increased in PWH with glucose intolerance (prediabetic and diabetic) compared with non-diabetic PWH (median proportion 1.0% vs 0.4%; $p < 0.001$). Finally, we identify classical monocytes by expression of *VAN, S100A8, S100A12*, non-classical monocytes by expression of *FCERG1A, SIGLEC10,* and a third monocyte group expressing *FCN1, APOBEC3A,* and *SERPINA1*.

LAMs undergo dramatic expansion with obesity, but it is unknown whether LAMs increase in the setting of type 2 diabetes and HIV infection. Strikingly, diabetic PWH, HIV-negative diabetics, and pre-diabetic PWH had higher LAMs as a proportion of total myeloid cells compared with non-diabetic PWH (median proportion 35.9% versus 17.3%, respectively, $p < 0.001$), highlighting an increase with metabolic disease regardless of HIV status (**Figure 2E**).

Non-diabetic PWH had a similar BMI compared with prediabetic PWH (31.0 vs. 29.4 kg/m^2, respectively; $p = 0.63$), indicating that the observed difference was not attributable to adiposity alone. This relationship remained significant after controlling for age, BMI, sex, and HIV serostatus using ordinal linear regression. While the proportion of LAMs increased, the ratio of PVMs did not vary by metabolic status (**Figure 2E)**. Instead, classical monocytes (*VCAN, S100A8, S100A9*) decreased with an increasing proportion of LAMs ($\rho = -0.71$, $p < 0.001$) (**Figure S2D**). LAMs and PVMs accounted for the increasing proportion of myeloid cells observed with progressive glucose intolerance (HIV+ non-diabetic 36.8%; HIV+ prediabetic 45.6%; HIV+ diabetic 52.1%; HIV-negative diabetic 53.4%). LAMs mainly accumulate through the recruitment of monocytes (Jaitin et al., 2019), while local proliferation may contribute to the accumulation of CD11c$^+$ macrophages (Amano et al., 2014; Russo and Lumeng, 2018). We found that LAMs accounted for nearly all proliferating macrophages, suggesting that local proliferation may have a role in maintaining or expanding LAMs (**Figure 2C**). We further compared the gene expression pattern of all macrophages between diabetic PWH and non-diabetic PWH (**Figure 2F**). Diabetic PWH had higher expression of lipid processing genes, including *TREM2, FABP5, APOE, CD9,* and *SSP1*, and reduced expression of *CCL2, KLF2, KLF4,* and *TGFBI,* consistent with an expansion of LAMs. Comparing LAMs between diabetic and non-diabetic PWH showed few gene expression differences, suggesting that LAMs have similar gene expression in diabetic and non-diabetic PWH but differ in proportions (**Table S4**).

Given our finding of an increasing LAM proportion with progressive glucose intolerance, we next evaluated whether a similar difference was present in whole adipose tissue gene expression. We used the NanoString nCounter platform to assess the expression of 249 genes related to inflammation and immune signaling in cryopreserved whole adipose tissue samples

from 85 individuals who also had scRNA-seq. We used a linear regression model with gene expression as the outcome and the proportion of LAMs as the independent variable, adjusted for age, BMI, diabetes status, batch, and sex (see STAR Methods). We found that *TREM2* expression, a marker of LAMs and critical for LAM function, was the top gene associated with the LAM proportion (p-value < 0.001 after adjustment for multiple comparisons), confirming that accumulation of LAMs is detectable in whole tissue gene expression (**Table S5**). Taken together, LAMs accumulate with glucose intolerance irrespective of HIV serostatus and account for nearly all proliferating macrophages, suggesting local expansion as a possible mechanism for accumulation.

A recent report described a novel intermediate macrophage subtype in scWAT, enriched in obesity, which is $CD206^{-}$ $CD11C^{+}$ with the expression of inflammatory markers such as *CXCL2*, *CXCL3*, and *TNF* (Hildreth et al., 2021). Using the Seurat module score function including genes expressed > two-fold in this novel macrophage subset, the cluster labeled monocyte-macrophage subset is transcriptionally most similar to this intermediate macrophage phenotype (**Figures S2E and S2F**). Notably, we did not detect differences in the proportion of the monocyte-macrophage subset with glucose intolerance or HIV serostatus (**Figure 2E**).

$CD4^{+}$ and $CD8^{+}$ T Effector Memory Cells Accumulate with Glucose Intolerance

Lymphoid cells have a prominent role in shaping immune responses in scWAT and modulate local inflammation and insulin resistance (Cipolletta et al., 2012; Deiuliis et al., 2011; Fabbrini et al., 2013; Feuerer et al., 2009; Kahn et al., 2019; Winer et al., 2009). In parallel, HIV infection induces broad changes to circulating lymphoid cells associated with the development of insulin resistance, including depletion of naïve $CD4^{+}$ T cells, persistent activation of $CD4^{+}$ and

$CD8^+$ T cells, and expansion of memory, senescent, and exhausted phenotypes (Appay and Sauce, 2008; Bofill et al., 1996; Day et al., 2006; Hazenberg et al., 2000; Wanjalla et al., 2019). There are fewer studies on adipose tissue T cells in the context of metabolic disease.

We performed focused analyses of lymphoid cells (n = 31,140 cells excluding B cells and plasmablasts) in isolation and in relation to other immune cells as part of this comprehensive atlas (**Figure 3A**). We identified 16 distinct cell states including: $CD4^+$ & $CD8^+$ naïve (*SELL, LEF1, CCR7*), central memory (T_{CM}) (*LTB, LDHB, GPR183*), T_{EM} (*ALOX5AP, COTL1, CCL5*), cytotoxic T_{EMRA} and senescent (*NKG7, GNLY, PRF1*), and $CD4^+$ T_{reg} (*FOXP3, CTLA4*) cells. Additionally, we identified γδ T cells (*TRDV1, KLRC2*), MAIT cells (*CCR6, IL7R, KLRG1*), and ILCs *(XCL1, KIT, IL7R*). Several NK cell subsets were identifiable by cell-surface expression of CD16 and CD56 and included mature $CD16^+$ (*FCER1G, NKG7)*, terminally differentiated mature $CD16^+CD57^+$ (*FCGR3A, KLRD1*), and $CD56^+CD16^-$ (*XCL1, XCL2, SELL*) (**Figures 3B and S3A; Table S3**). The RNA transcriptomes profiles were analyzed in parallel with CITE-seq surface marker expression of CD4, CD8, CD45RA, CD27, CD45RO, CD57, and CD16 (**Figure 3C**).

Comparison of cell proportions in the lymphoid compartment revealed several changes specific to diabetes and HIV serostatus (**Figure 3D**). The majority of scWAT T cells were $CD8^+$ in non-diabetic PWH (61.2%), prediabetic PWH (69.2%), and diabetic PWH (59.1%), whereas the majority of T cells were $CD4^+$ in diabetic HIV-negative individuals (58.5%). This finding is consistent with previous studies that found PWH have circulating $CD8^+$ T cell inflation, and adipose tissue is enriched for late differentiated $CD8^+$ T cells (Couturier et al., 2015; Wanjalla et al., 2019). In the NK compartment, HIV-negative diabetics had a higher proportion of immature NK cells as a total percentage of lymphoid cells compared with diabetic PWH (5.8% vs. 3.8%

respectively, p = 0.02). There was a lower proportion of terminally differentiated $CD57^+$ mature NK cells compared with all PWH (9.9% vs. 14.4% respectively, p = 0.01), but no difference compared with diabetic PWH alone. Similarly, the γδ T cell proportion was lower in HIV-negative diabetics compared with all PWH (2.0% vs. 4.1% respectively, p = 0.008) but not compared with diabetic PWH alone.

We have previously shown that in diabetic PWH, but not diabetic HIV-negative individuals, adipose tissue is enriched for $CD4^+$ T_{EM} and T_{EMRA} cells co-expressing CX3CR1, GPR56, and CD57 (Wanjalla et al., 2021). We assessed $CD4^+$ and $CD8^+$ T cells separately to evaluate the T cell compartment. A total of 8,045 cells were classified as CD4+ T cells by transcriptional profile and CITE-seq surface marker phenotype (**Figures S3B-S3E**). $CD4^+$ T_{CM} and T_{EM} accounted for most of the scWAT $CD4^+$ T cell compartment in PWH and HIV-negative individuals (**Figure S3E**). There was no difference in the proportion of $CD4^+$ T_{EM} between diabetic PWH and HIV-negative diabetics (45.4% vs. 47.0% respectively, p = 0.58). $CD4^+$ T_{EMRA} and senescent cell proportions were higher in diabetic PWH compared with HIV-negative diabetics (13.4% vs 4.2% respectively, p = 0.02). The proportion of $CD4^+$ T_{REG} cells was not significantly different between diabetic PWH and HIV-negative diabetics (4.7% vs. 6.4% respectively, p = 0.12). However, the proportion of $CD4^+$ T_{EM} was increased in pre-diabetic and diabetic PWH compared with non-diabetic PWH (44.3% vs 22.6% respectively, p = 0.05). There was no difference in the proportion of $CD4^+$ T_{EMRA} and senescent cells by metabolic status in PWH.

A total of 11,325 cells were classified as $CD8^+$ T cells by transcription profile and CITE-seq (**Figures S3F-S3I**). $CD8^+$ T_{EMRA} and senescent cells comprised most of the $CD8^+$ T cell compartment, which did not differ by HIV serostatus. The $CD8^+$ T_{EM} proportion increased

between prediabetic and non-diabetic PWH (38.1% vs 23.9% respectively, $p = 0.02$) but not between diabetic and non-diabetic PWH (37.5% vs 23.9% respectively, $p = 0.69$).

Lymphoid cell populations had similar gene expression when we compared diabetic PWH with diabetic HIV-negative persons and when we compared diabetic PWH with non-diabetic PWH (**Tables S4**). In summary, $CD4^+$ and $CD8^+$ T_{EM} proportions increase with glucose intolerance in PWH. PWH have a dramatic increase in the proportion of lymphoid cells in adipose tissue compared with HIV-negative persons, accompanied by a preferential accumulation of $CD8^+$ T cells.

$CD4^+$ and $CD8^+$ T Effector Memory Cells and Lipid-Associated Macrophages are Correlated in Persons with HIV

Adipose tissue T cells and macrophages interact to modulate local inflammation. In the context of metabolic disease, $CD11c^+$ macrophages can act as antigen-presenting cells and promote $CD4^+$ T cell activation through major histocompatibility complex class II (Cho et al., 2014; Morris et al., 2013). In addition, T cells are crucial for recruiting macrophages to the adipose tissue (Nishimura et al., 2009). We assessed whether LAMs (as a proportion of total myeloid cells) correlate with $CD4^+$ and $CD8^+$ T_{EM} cells (as a proportion of total $CD4^+$ and $CD8^+$ T cells, respectively) and whether the relationship differs by metabolic status and HIV serostatus. The spearman's ρ between LAMs and $CD4^+$ T_{EM} cells in PWH was 0.67 ($p < 0.001$) and remained significant after adjusting for BMI, age, and metabolic status ($\rho = 0.53$ [0.24, 0.73], $p < 0.001$) (**Figure 3E**). In contrast, there was no significant correlation between LAMs and $CD4^+$ T_{EM} cells in HIV-negative persons ($\rho = -0.2$, $p = 0.43$) (**Figure 3E**). The proportion of $CD8^+$ T_{EM} cells was also significantly correlated with the LAM proportion in PWH ($\rho = 0.63$, $p < 0.001$),

and remained significant, though attenuated, after adjusting for BMI, age, and glucose intolerance (ρ = 0.42 [0.10, 0.67], p = 0.01). There was no association between $CD8^+$ T_{EM} cells and LAMs in HIV-negative persons (ρ = 0.07, p =0.80) (**Figures 3F**). Taken together, these data show a strong relationship between LAMs and $CD4^+$ and $CD8^+$ T_{EM} cells in the adipose tissue of PWH only, which may indicate either a shared driver of cell accumulation or enhanced importance of T cells in the recruitment of LAMs in PWH.

White Adipose Tissue Contains Distinct Adipogenic and Fibroblast Cell Populations

Fibrogenic and adipogenic cells in humans have not been well characterized to date, but several recent studies have identified functional diversity in adipogenic cells in both mice and humans (Burl et al., 2018; Merrick et al., 2019; Min et al., 2019; Oguri et al., 2020; Sarvari et al., 2021; Schwalie et al., 2018; Sun et al., 2020; Vijay et al., 2020). Interactions between stromal cells and immune cells can modulate adipocyte function and have an important role in the development of metabolic disease (Brestoff et al., 2021; Russo and Lumeng, 2018). We performed focused analyses of the stromal cell compartment (n = 87,674 cells), and observed several distinct adipocyte stem cells (ASC), fibroblasts, and preadipocyte populations (**Figure 4A; Table S3**). There is no single consensus marker for progenitors and preadipocytes *in-vivo* (Ghaben and Scherer, 2019), and several overlapping populations have been described in mice and subsequently reported in humans. We identified three cell populations expressing ASC markers, including *DCN, CLU, LUM, GSN,* and *PI16* (**Figures 4B, S4A, and S4B**). ASC 1 expresses several immediate early genes (IEG) (*MYC, FOS, JUN)* and markers associated with adipogenesis and regulation of inflammation (*ZFP36, EGR1, KLF4, CEBPD)* (Brahma et al., 2012; Ghaben and Scherer, 2019; Lee et al., 2019; Urs et al., 2004*)*. The preadipocyte

compartment clusters by differences in the relative expression of these same markers (**Figure S4B)**. The preadipocytes progressively acquire higher expression of *FABP4*, *LPL*, and *CIDEC*, which are markers of lipid acquisition. Preadipocytes lacking expression of IEG have higher expression of extracellular matrix (ECM) proteins. One cluster that expresses CD9 appears similar to a previously described pro-fibrotic population (Marcelin et al., 2017). These ECM-producing preadipocytes were closely associated with cluster ASC 3 (**Figure 4A**). Gene Ontology over-representation analysis of each preadipocyte population demonstrates unique pathway over-representation: ECM organization in CD9hi preadipocyte, ECM-producing preadipocyte, and PTGDS^{+} ECM-producing preadipocyte; fat cell differentiation in early preadipocytes; and lipid metabolism in mature preadipocytes (**Figure S4C**). A cluster of preadipocytes (mixed with ASC) express metallothionein genes, and a separate cluster express *ISG15* and other IFN-related genes (**Figure 4A**). Finally, we identified several fibroblastic cell populations similar to those recently described in the dermis (Tabib et al., 2021). One population expressing *SFRP2*, *DPP4*, and *PCOLCE2* is analogous to the *PCOLCE+* fibroblast. A second population has high expression of *MYOC* and *ITM2A* similar to the *MYOC*$^{+}$ fibroblast, and a third population expressing *TIMP1* and *POSTN* are consistent with a myofibroblast. The expression of DKK3 characterized a final population.

We next compared our cell populations with annotations from other studies predominantly performed in mice. Merrick *et al*. described interstitial *DPP4+* progenitor cells that give rise to preadipocytes which correspond to *POLEC+* fibroblast and ASC 3 populations in our analysis, whereas ICAM+ preadipocyte cells correspond with preadipocytes in our analysis (**Figure S4D) (**Merrick et al., 2019**)**. Similarly, we observed that the adipogenic clusters described by Schwalie *et al.* (**Figure S4E)** and Sarvari *et al.* (**Figure S4F)** overlap with distinct

clusters in our dataset (Sarvari et al., 2021; Schwalie et al., 2018). Taken together, we uncovered significant diversity in human fibro-adipogenic cell populations and more finely characterized cell populations previously identified in prior smaller human or murine studies.

Lipid-Associated Macrophage Accumulation in PWH and HIV-negative Individuals is Associated with Increased Stromal Myofibroblasts.

We next assessed stromal cell composition and found similar subset proportions across our study groups (**Figure 4C**). As most participants were obese and all had either HIV, glucose intolerance or both, this suggests that the relative composition of the adipose stromal tissue may be conserved in these populations. Resident immune cells, particularly macrophages, have an important role in promoting adipose tissue inflammation, recruitment of fibroblasts, myofibroblasts, and fibrosis (Sun et al., 2013). Given that both HIV and obesity are associated with adipose tissue fibrosis (Halberg et al., 2009), we next assessed whether the accumulation of LAMs was associated with a higher proportion of myofibroblasts and fibroblastic progenitors. LAMs as a proportion of total myeloid cells and myofibroblast as a proportion of total stromal cells were highly correlated (ρ =0.72; $p < 0.001$) (**Figure 4D**). This remained significant when evaluating only PWH ($\rho = 0.71$, $p < 0.001$) and only HIV-negative persons ($\rho = 0.79$, $p < 0.001$), and after adjustment for age, BMI, and metabolic status in a regression model ($\rho = 0.71$ [0.55, 0.82], $p < 0.001$). The $CD4^+$ T_{EM} cell proportion was also correlated with the myofibroblast proportion in PWH only ($\rho = 0.35$; $p = 0.03$), but was not significant after adjusting for age, BMI, and metabolic status ($\rho = 0.28$ [-0.3, 0.54], $p = 0.08$) (**Figure 4E**). Similarly, the proportion of $CD8^+$ T_{EM} cells was correlated with the myofibroblast proportion in PWH only ($\rho = 0.42$; $p = 0.004$), though this was not significant after adjusting for age, BMI, and metabolic status (ρ =

0.27 [-0.05, 0.54], p = 0.09) (**Figure 4F**). Finally, the LAM proportion was correlated with the CD9hi preadipocyte proportion after adjusting for age, BMI, metabolic status, and HIV serostatus ($\rho = 0.27$, $p = 0.02$). Taken together, our data suggests that LAM accumulation occurs alongside the expansion of myofibroblasts and pro-fibrotic progenitor cells.

Discussion

Type 2 diabetes and other metabolic disorders are increasingly prevalent worldwide and contribute to substantial morbidity and mortality. Alterations in adipocyte function and adipose tissue immune cell populations in PWH may underlie the increased risk for metabolic disease in these individuals compared with HIV-negative persons. scWAT is a critical regulator of metabolic hemostasis through local and systemic effects mediated by complex interactions between stromal and immune cells. In this study, we generated the most comprehensive single-cell molecular atlas of scWAT in humans to date. We characterized the immune cell and stromal cell composition with HIV infection and glucose intolerance. We report the unique and shared polarization of macrophages and T cells in PWH and HIV-negative individuals with diabetes. We further describe adipogenic precursors in greater detail than previously characterized and link compositional changes to macrophage polarization in the setting of glucose intolerance. These findings provide a basis for further research on the role of adipose tissue immune cells, including potential therapeutic avenues, in metabolic disease in PWH and, more broadly, in the general population.

Our characterization of scWAT resident immune cells and fibro-adipogenic precursor cells expands on the previous scRNA-seq description of human adipose tissue (Hildreth et al., 2021; Vijay et al., 2020). We found a dramatic increase in the proportion of LAMs with glucose

intolerance regardless of HIV serostatus. Additionally, we found that the proportion of PVMs remained stable, resulting in an overall increase in the macrophage compartment and decreased proportions of monocytes, which is consistent with some studies (Fuchs et al., 2021), but not all (Hildreth et al., 2021; Jaitin et al., 2019). The precise role of LAMs in adipose tissue inflammation and metabolic disease remains unclear. $CD11c^+$ cells have been associated with an activated and inflammatory state, with several studies linking these cells with worse metabolic outcomes (Cho et al., 2014; Lumeng et al., 2007a; Patsouris et al., 2008). More recent work found that LAMs (also $CD11c^+$) reduce adipocyte hypertrophy, improve insulin resistance, and are critical for forming crown-like structures that may minimize inflammation in a hypoxic tissue environment (Jaitin et al., 2019). The broad expression of CD11c could partly explain this discrepancy in different cell types (Russo and Lumeng, 2018).

Given our study cohort's cross-sectional nature, we cannot determine the direct role of LAMs in the development of adipose tissue inflammation and metabolic disease in humans. Intriguingly, despite our cohort including only overweight and obese individuals, glucose-intolerant individuals had a more significant accumulation of LAMs compared with non-diabetic individuals, suggesting that the differences in adipose tissue environment are independent of obesity. In Hildreth *et al.*, the proportion of LAMs increased with obesity but represented a much smaller macrophage subset compared with intermediate macrophages (Hildreth et al., 2021). In our study, the proportion of monocyte-macrophages (most similar to intermediate macrophages from Hildreth's study) did not change with HIV infection or glucose intolerance and represented a much smaller proportion of overall macrophages. The reasons for this difference are not clear, but may be due to different index sorting strategies in other studies, higher rates of obesity in all comparison groups, and the inclusion of individuals with type 2 diabetes in our study.

To our knowledge, this is the first proteogenomic characterization of human scWAT T cells from living donors with concomitant metabolic phenotyping. We found that participants with HIV had a greater proportion of adipose tissue T cells and NK cells than HIV-negative individuals. This was driven primarily by preferential $CD8^+$ T cell accumulation relative to $CD4^+$ T cells in PWH, consistent with previous flow cytometry analyses of adipose tissue in PWH (Couturier et al., 2015; Damouche et al., 2015; Wanjalla et al., 2019). While there was a global increase in T cells, the overall distribution of T cell subsets was relatively conserved between diabetic PWH and diabetic HIV-negative persons. We could not resolve CX3CR1 or GPR56 expression to identify $CD4^+$ $CX3CR1^+$ $GPR56^+$ $CD57^+$ cells that have previously been associated with glucose intolerance in PWH (Wanjalla et al., 2021). However, the majority of these cells are likely contained within the $CD4^+$ T_{EM} and T_{EMRA} populations. Both $CD4^+$ and $CD8^+$ T_{EM} proportions correlated with LAMs in PWH but not HIV-negative participants. $CD4^+$ and $CD8^+$ T_{EM} cells can recruit and polarize macrophages towards a $CD11c^+$ inflammatory macrophage subtype (Cho et al., 2014; Nishimura et al., 2009). One intriguing possibility is the presence of antigenic stimuli promoting $CD4^+$ and $CD8^+$ infiltration in PWH, potentially related to the known role of adipose tissue as a reservoir of replication-competent HIV despite plasma viral suppression, or a response to CMV reservoirs that may be inflated in PWH versus HIV-negative persons (Abana et al., 2017; Couturier et al., 2015; Wanjalla et al., 2021). Future prospective studies evaluating TCR antigen specificity, viral reservoir measurements, and functional assays are needed to assess viral-specific T cell responses in adipose tissue.

To date, scWAT fibro-adipogenic cells remain poorly characterized, hindering our understanding of how interactions between stromal and immune cells regulate metabolic fitness (Hildreth et al., 2021; Merrick et al., 2019; Min et al., 2019; Vijay et al., 2020). Conventional

adipocyte progenitor markers identified *in vitro* do not correspond to transcriptionally distinct cell clusters *in vivo* (Ghaben and Scherer, 2019). We overcame this limitation by generating a sizeable fibro-adipogenic atlas that enabled detailed resolution of cell types. Many of these populations shared similar features to those identified in previous studies in both mice and humans. Interestingly, individuals with a higher LAM proportion have an increased proportion of myofibroblasts and a distinct pro-fibrotic cluster previously linked to obesity-related fibrosis and attenuation of normal adipogenesis (Marcelin et al., 2017). This finding remained significant after adjusting for glucose intolerance, suggesting that the proportion of LAMs may reflect the degree of inflammation and fibrosis in adipose tissue.

This study has several strengths. To date, this is the largest single-cell dataset for human adipose tissue, including 91 individuals and approximately 283,000 cells, which provided substantial power to characterize differences between disease states and cell types. Additionally, all participants are part of an ongoing longitudinal study on the contribution of inflammation and immune activation to the development of metabolic disease in PWH, with the collection of a wide range of clinically important variables. In contrast to prior single-cell studies in human adipose tissue primarily focused on obesity, this study was designed to uncover compositional and transcriptional differences between type 2 diabetes and HIV infection. With this cohort, we are uniquely able to utilize immune cell alterations associated with HIV infection and compare them with HIV-negative individuals to uncover potential drivers of adipose tissue dysfunction that promote glucose intolerance. Our analysis approach employed a rigorous strategy to remove homotypic and heterotypic cells and retain high-quality cells to decrease noise. Finally, our dataset is publicly available to the research community to enable further studies and advance our understanding of adipose tissue and its role in metabolic homeostasis.

There are also several important limitations to this study. Our design is cross-sectional, so we cannot determine the temporal course of compositional changes in the adipose tissue as it relates to HIV infection or the development of metabolic disease. Future longitudinal scRNA-seq studies will be needed in prospective cohorts to explore these relationships. Additionally, this cohort lacked an HIV-negative non-diabetic group. An inherent limitation of droplet-based scRNA-seq platforms is that there is limited power to detect differences in genes with critical biological roles but have low mRNA expression. Additionally, scRNA-seq does not capture mature adipocytes, which are better studied with single-nuclei RNA-seq. However, we would be unable to perform paired CITE-seq with single-nuclei RNA-seq for accurate characterization of immune cells so we chose scRNA-seq for this study.

Our study generated the most extensive and detailed single-cell transcriptomic and proteomic molecular atlas of scWAT in a well-phenotyped, living human cohort to date. Our investigation uncovered a diversity of immune and stromal cells associated with clinical disease conditions at a level of resolution not previously demonstrated. These data provide insight into the complexity and breadth of scWAT cells that may contribute to glucose intolerance and accelerate future investigation into the role of stromal and immune cell interactions that may open new avenues of research and lead to the development of therapeutic interventions.

Methods

Study Participants. Participants were members of the HIV, Adipose Tissue Immunology, and Metabolism (HATIM) study developed to evaluate adipose tissue characteristics in the context of HIV infection and metabolic disease (ClinicalTrials.gov registration NCT04451980). PWH were recruited from the Vanderbilt University Medical Center Comprehensive Care Clinic between August 2017 and June 2018, and were on antiretroviral therapy (ART) for ≥ 18 months, had virologic suppression (serum HIV-1 RNA quantification < 50 copies/mL) for ≥ 12 months, had a $CD4^+$ T cell count ≥ 350 cells/mm^3 and had no known inflammatory or rheumatologic conditions. Participants were classified as non-diabetic (HbA1c < 5.7% and/or fasting blood glucose [FBG] < 100 mg/dL), pre-diabetic (HbA1c 5.7-6.5% and/or FBG 100-125 mg/dL), or diabetic (HbA1c > 6.4% and/or FBG ≥ 126 mg/dL and/or on anti-diabetic medication) in accordance with the American Diabetes Association criteria (American Diabetes, 2020). HIV-negative participants with diabetes were simultaneously recruited from the Vanderbilt *ResearchMatch* cohort, and these individuals were group matched by age and BMI with diabetic PWH. All participants underwent a single clinical research visit after a minimum 8 hour fast that included HbA1c and FBG measurement, peripheral blood mononuclear cell (PBMC) collection, fasting plasma collection, and anthropomorphic measurements. All individuals also underwent subcutaneous adipose tissue liposuction as described below. The Vanderbilt Institutional Review Board approved the research, and all participants provided written consent.

Adipose Tissue Collection and Processing. Subcutaneous adipose tissue biopsies were collected approximately 3 centimeters to the right of the umbilicus after anesthetizing the skin with lidocaine/epinephrine and infiltrating 40 mL of sterile saline and lidocaine into the SAT.

We collected approximately 5 grams of adipose tissue using a 2.1 mm blunt, side-ported liposuction catheter (Tulip CellFriendly™ GEMS system Miller Harvester, Tulip Medical Products) designed for extraction of viable adipocytes and stromal vascular fraction (SVF) during cosmetic adipose tissue transfer procedures (Alexander and Harrell, 2013). Using this method, adipose tissue is recovered in droplets generally < 3 mm in diameter, limiting the need for mechanical dissociation. The tissue was placed in 40-50 mm^3 of cold saline and mixed. Visible blood clots were removed, and the sample was transferred to a 70 µm filter for repeat saline washes with constant stirring. The adipose tissue was then placed in a gentleMACS™ Dissociator (Miltenyi Biotec) followed by incubation with 100 µL of collagenase D (20mg/mL). The SVF was separated using a Ficoll-Paque Plus density gradient. Samples were cryopreserved in fetal bovine serum with 10% DMSO in liquid nitrogen.

Library Preparation and Sequencing. An antibody Total Seq C master mix containing 45 common markers for lineage, memory, and activation was created by adding 0.5 µL of each antibody. Twelve samples, with representative samples from the four metabolic groups (non-diabetic PWH, pre-diabetic and diabetic PWH, and HIV-negative diabetics), were processed at a single time. The samples were quickly thawed and transferred to labeled 15 mL tubes and diluted to 10 ml with phosphate-buffered saline (PBS) before spinning down at 300 G for 10 minutes. The supernatant was aspirated, and the pellet was resuspended in cell staining buffer and transferred to labeled flow tubes. The sample was again spun at 300 G for 10 minutes, and the supernatant was aspirated. Cells were resuspended in 100 µL of staining buffer. Human TruStain FcX Receptor Blocking Solution (5 µL) was added to the tube and incubated at 4 Celsius for 10 minutes. The antibody master mix was spun at 15000 rpm for 5 minutes to remove any

aggregates that had formed, and 22.5 µL of the antibody mix was added to each tube of cells and mixed by flicking the tube. A total of one µL of Total Seq C hashtag antibody was added to the samples, and the samples were incubated at 4 Celsius for 30 minutes. After incubation, the cells were washed three times with Cell Staining Buffer and spun at 300 G for 10 minutes. The cells were resuspended in around 100 µL of PBS with 0.04% bovine serum albumin (BSA). The cells were counted using the Countess II Automated Cell Counter (Thermo Fisher) to determine the suspension volume to transfer to obtain 5,000 cells. Four samples (each with a unique hashtag antibody) were pooled by metabolic status (except non-diabetic and preadiabetic samples from PWH which were pooled) together into one tube. The multiplexed single-cells were loaded onto a Chromium Single Cell 5' v.3 assay (10x Genomics). Libraries were sequenced on the NovaSeq 6000 S2 platform (Illumina) with 50 bp paired-end reads. Illumina bcl files were demultiplexed using bcl2fastq. Raw reads were then aligned to the human genome (hg38) using STAR v. 2.7.2a, and cells were called using cellranger count (v.6.0.0) using default settings. Souporcell, which leverages single nucleotide variants to assign individual cells to genotypes and generate a VCF file, was used to genetically demultiplex the samples (Heaton et al., 2020). SoupX was used with default parameters to remove ambient RNA contamination from the count matrices (Young and Behjati, 2020).

Quality Control. The R Statistical Programming package Seurat V4 was used to further process the scRNA-seq data (Stuart et al., 2019). First, cells with > 25% mitochondrial gene expression, < 800 transcript reads, and < 200 genes were filtered out. The threshold of 800 transcript reads per cell was selected because the performance of Souporcell begins to decrease with fewer transcripts (Heaton et al., 2020). Hashtag oligonucleotides (HTOs) were normalized using

centered log-ratio (CLR) transformation, and cells were assigned HTO implemented in the function HTODemux with default parameters (Stoeckius et al., 2017; Stoeckius et al., 2018). We then added the Souporcell assignment to the metadata and linked the Souporcell cluster designation with the HTO classification, forming a link with the metadata. All cells that were identified as doublets or unassigned by Souporcell were removed. To identify heterotypic doublets, we used standard processing of each lane, including normalization and variance stabilization using regularized negative binomial regression (SCTransform), dimensional reduction, and clustering (Hafemeister and Satija, 2019). DoubletFinder (McGinnis et al., 2019) was used to identify potential heterotypic doublets in the data. Clusters that expressed transcripts from multiple major lineages (endothelial, immune, stromal) and/or were identified by DoubletFinder as doublets were labeled for removal after integrating the datasets.

Cell Clustering and Annotation. Processed individual lanes were merged using the merge function. The gene counts were normalized for each cell by dividing by the total gene counts and multiplying by a factor of 10,000 before applying log-transformation as implemented by the LogNormalize function. Protein expression counts were normalized using the CLR method. Variable genes were identified using the FindVariableFeatures function (nFeatures = 3000), and the data were scaled and centered using the ScaleData function. Principal component analysis (PCA) was performed on the scaled data. The number of principal components (PCs) used for downstream analysis was selected based on elbow plots and heat maps of PC dimensions as implemented in the DimHeatmap function. To reduce the batch effect associated with running multiple 10X lanes, we used the Harmony algorithm on the uncorrected PCA implemented as a Seurat wrapper to integrate across lanes (Korsunsky et al., 2019). We performed clustering on

the Harmony-corrected PCs using FindNeighbors and FindClusters functions. Marker genes for each cluster were determined using the Model-based Analysis of Single Cell Transcriptomics (MAST) wrapper implemented in FindAllMarkers (Finak et al., 2015). The integrated dataset was then subclustered as described below. After processing each subcluster, they were merged again, and the process described above (except normalization) was repeated to obtain a cell atlas of the scWAT. We performed manual annotation of cell populations based on canonical markers and markers previously identified in scRNA-seq (Table S1).

Subclustering Analysis. We subclustered on major cell types, including stromal (*COL1A2*), vascular (*CLDN5, ACTA2*), myeloid (*LYZ, CD68, CD14, CD1C, LILRA4, CLEC9A*), and lymphoid (*CD3, NKG7*). We followed the procedure described previously for each subcluster but did not repeat RNA and protein normalization. Clusters defined by mitochondrial gene expression and/or were transcriptional doublets were removed from the analysis. We compared cell composition between disease states for each subcluster by evaluating each cell type as a proportion of total cells in the subcluster. We assessed whether cell type changes were significant between diabetic PWH and diabetic HIV-negative persons and diabetic PWH and non-diabetic PWH using Wilcoxon rank sums with a p-value < 0.05 as significant.

To evaluate the relationship of $CD4^+$ and $CD8^+$ T_{EM} and T_{EMRA} cells with LAMs, we subclustered on $CD3^+$ T cells with $CD8^+$ protein expression ($CD8^+$ T cells) and T cells without $CD8^+$ protein expression ($CD4^+$ T cells). Individuals contributing less than 30 cells were excluded from the analysis. Spearman's correlation was performed between $CD4^+$ T_{EM} as a proportion of total $CD4^+$ T cells and LAMs as a total proportion of myeloid cells. Spearman's correlation was performed between $CD8^+$ T_{EM} as a proportion of total $CD8^+$ T cells and LAMs as

a total proportion of myeloid cells. We performed partial Spearman correlation adjusting for age, BMI, and glucose intolerance status implemented in the R package 'PResiduals' (Lui et al., 2020). We performed the same analysis to evaluate the relationship between LAM and myofibroblast and $CD4^+$ or $CD8^+$ T cells and myofibroblast.

Differential Gene Expression Analysis. We performed differential gene expression using the FindAllMarkers function implemented in Seurat to identify gene markers for each cell population. We used MAST implemented as a wrapper function and included genes expressed in at least 25% of cells with a $\log_2$ fold change of 0.25 or greater. We used ClusterprofileR to perform over-representation analysis of Gene Ontology (GO) biological processes pathways with gene markers with an FDR-adjusted p-value < 0.05 for each cell cluster used as input. Simplify was used to remove redundant GO pathways. The top 5 pathways for each cluster with FDR-adjusted p-value < 0.05 were used for plotting.

Differential gene expression analysis was also performed between diabetic PWH and diabetic HIV-negative persons and between diabetic PWH and non-diabetic PWH. We used the MAST wrapper implemented in the function FindAllMarkers and included genes expressed in at least 25% of cells with a $\log_2$ fold change of 0.25 or greater. We adjusted for age, sex, and BMI.

Reference Label Transfer. Raw FASTQ files from macrophage and sorted dendritic cells (Hildreth *et al.)* were downloaded from Gene Expression Omnibus (GEO) (accession number GSE156110). The FASTQ reads were aligned to the GRCh38, and cells were called using cellranger count (v6.0.0). Cells with less than 500 reads or more than 25% mitochondrial gene expression were removed from the analysis. The Harmony algorithm was applied to the principal

component matrix, which was used for downstream clustering. The myeloid subset generated in the current paper was used as the reference dataset. We used the FindTransferAnchors function in Seurat with projection of the reference PCA onto the query dataset to identify anchors (cell pairs) between the datasets. We then used this defined anchor set in the TransferData function to transfer annotation labels to the query dataset. We used genes expressed 2-fold or greater in the intermediate macrophage from Hildreth *et. al.* as input to the Seurat module score function (49 genes).

Pseudotime Analysis. The R package Slingshot (Street et al., 2018) was used to assess the pseudo-time trajectory of endothelial to mesenchymal transition of capillary cells to pericytes. Capillary, intermediate, and pericyte cells were subclustered as described previously. Capillary cells were specified as the root cluster with the dimensionality reduction produced by UMAP. To identify temporally dynamic genes, we fit a generalized additive model (GAM) using a negative binomial additive model implemented in the R package tradeSeq (Van den Berge et al., 2020). We used the associationTest function with l2fc set to 2 to identify genes significantly changing along the pseudo-time, defined as FDR-adjusted p-value < 0.05. The genes were then ordered according to pseudo-time and plotted by scaled expression using ComplexHeatmap (Gu et al., 2016).

Whole Adipose Tissue Messenger RNA Expression. The detailed methods for these samples have been published elsewhere (Gabriel et al., 2021). Briefly, messenger RNA (mRNA) was extracted from cryopreserved scWAT with Qiagen RNeasy Lipid Tissue Kit after mechanical lysis. The NanoString nCounter Plex platform (NanoString, Seattle, WA) was used to quantify

mRNA transcripts for 249 genes related to inflammation from the inflammation panel. The mRNA count was normalized using eight synthetic spike-ins for negative control and six synthetic spike-ins for positive controls. The coefficient of variation (CV) was calculated for control genes. First, the mean of the negative controls was used as the background level and subtracted from each gene count. The normalization factor for the mRNA content was calculated using the geometric mean of a set of pre-specific housekeeping genes. The count data were then divided by the normalization factor to generate counts normalized to the geometric mean of housekeeping genes. The normalized gene count data was then log2-transformed, and a linear regression model was used to assess the relationship between the proportion of LAMs with mRNA expression. The proportion of LAMs was the independent variable, and the log2-transformed mRNA count was the dependent variable, adjusted for age, sex, BMI, metabolic status, and batch. Benjimani-Hochberg was used to correct for multiple comparisons.

Data and Code Availability. The gene expression data generated from this study are deposited in the NIH Gene Expression Omnibus. The accession number for the sequences reported in this paper is GSE198809. The code for processing and analyzing this data and processed Seurat objects are available at https://github.com/VIMRG/AdiposeTissueAtlas. An interactive shiny app using Shiny Cell (Ouyang et al., 2021) is available at https://vimrg.app.vumc.org/vimrg.

Acknowledgments

This work was supported by National Institutes of Health grants R01DK112262 (JRK and CNW), R01HL145372 (JAK), K23HL156759 (CNW, JRK), the Vanderbilt Clinical and Translational Science Award from NCRR/NIH grant UL1RR024975, the Vanderbilt Infection Pathogenesis and Epidemiology Research Training Program (VIPER) grant T32AI007474, the Vanderbilt Scholars in HIV and Heart, Lung, Blood and Sleep Research (V-SCHoLARS) grant K12HL143956, the Vanderbilt Institute for Clinical and Translational Research supported by grant KL2TR002245 from the National Center for Advancing Translational Sciences, the Tennessee Center for AIDS Research grant P30AI110527 (SAM, CNW, JRK, SAK), the Doris Duke Charitable Foundation grant 2021193 (CNW, JRK) and the Burroughs Welcome Fund grant 1021480 (CNW, JRK). The funding authorities had no role in study design, data collection, analysis, interpretation, the decision to publish, or manuscript preparation. We also thank the participants of the HATIM study.

Author Contributions

Conceptualization, C.N.W., J.R.K., S.A.M.; Methodology, C.N.W., J.R.K., S.A.M., R.D.G., J.D.S., A.C., R.R., C.W., J.A.K., S.S.B.; Formal Analysis, S.S.B., C.N.W., J.R.K., S.A.K., J.A.K., R.R., F.Y., R.F.; Investigation, C.N.W., C.W., J.D.S., R.D.G., L.H.; Writing – Original Draft, S.S.B., C.N.W., J.R.K., J.A.K.; Writing – Review & Editing, S.S.B., C.N.W., J.A.K., J.R.K., S.A.M., S.A.K., C.L.G., M.M., L.H., J.D.S., C.W., R.F., F.Y.; Funding Acquisition, C.N.W., J.R.K., S.A.M.

Declaration of Interests

J.A.K. consults for Boehringer Ingelheim, Janssen, and Bristol-Myers-Squibb, serves on the scientific advisory board for APIE Therapeutics, and provides non-financial study support to Genentech. J.R.K. has served as a consultant to Gilead Sciences, Merck, ViiV Healthcare, Theratechnologies, and Janssen, and has received research support from Gilead Sciences and Merck. C.N.W. serves on the scientific advisory board for ViiV Health Care.

Main Figure Legends

Figure 1. Single-cell RNA sequencing reveals disease-specific heterogeneity of subcutaneous white adipose tissue. a, Schematic overview of study design. Twenty HIV+ non-diabetic, 19 HIV+ prediabetic, 20 HIV+ diabetic, and 32 HIV- diabetic participants underwent abdominal subcutaneous adipose tissue harvesting with liposuction. Tissue was processed with collagenase and dissociated. Single-cell suspensions from each participant were hashed and labeled with CITE-seq antibodies before multiplexing in groups of four. 10x libraries were generated using the Chromium platform and sequenced on Illumina NovaSeq 6000. The bioinformatic pipeline included demultiplexing, quality control, dimensional reduction and clustering, and differential gene testing. **b**, Uniform Manifold and Project (UMAP) of 283,491 cells from 91 individuals after removal of doublets and quality control, with manual annotation of cell clusters based on canonical gene markers. **c**, UMAP after harmony integration split by disease status showing successful integration; HIV+ non-diabetic (red), HIV+ prediabetic (orange), HIV+ diabetic (gold) and HIV- diabetic (blue). **d**, Gene expression projected on the UMAP identifying major cell types including stromal (*COL1A2, CCDC80*), vascular (*CLDN5, ACTA2*), myeloid (CD68, CD1C), T cell and natural killer cells (*CD3E, NKG7*). **e**, Boxplot showing the proportion of major cell categories (stromal, vascular, lymphoid, and myeloid) as a percentage of total cells split by disease status (HIV+ non-diabetic, red; HIV+ prediabetic, orange; HIV+ diabetic, gold; HIV- diabetic; blue). The horizontal black line represents the median, the box shows the lower and upper quartile limits and the whiskers are 1.5x the interquartile range.

Abbreviations: cMo, classical monocyte; cDC1, conventional dendritic cell type 1; cDC2B, conventional dendritic cell type 2B; DC, dendritic cell; EC, endothelial cell; ECM, extracellular matrix; EndoMT, endothelial-mesenchymal transitional; ILC, innate lymphoid cell; IFN+,

interferon; LAM, lipid-associated macrophage; Mac, macrophage; mNK, mature natural killer; Mo, monocyte; NK, natural killer; nMo, non-classical monocyte; pDC, plasmacytoid dendritic cell; PVM, perivascular macrophage; TEMRA, T effector memory RA; VSMC, vascular smooth muscle

Figure 2. Lipid-associated macrophages accumulate with glucose intolerance regardless of HIV serostatus. a, Uniform Manifold Approximation and Projection (UMAP) of myeloid cells (n = 68,631) from 91 individuals after subsetting and reclustering showing 12 distinct cell types/states. **b**, Dot plot showing selected gene markers on the x-axis and cell type on the y-axis. The dot size reflects the percentage of cells expressing the gene while the color reflects the scaled average expression. **c**, Violin Plot with macrophage subtype on the x-axis and scaled expression of *TREM2, CD9, RNASE1, LYVE1, HLA-DBP1, CXCL3, CXCL2, TIMP1,* and *ISG15*. **d**, Gene Ontology (GO) over-representation analysis with macrophage subtype on the x-axis and GO on the y-axis. The size of the circle denotes the negative $\log_{10}$ p-value while the color denotes the number of genes assigned to the pathway. **e**, Boxplot showing the proportion of each cell type as a percent of total myeloid cells split by disease state (HIV+ non-diabetic, red; HIV+ prediabetic, orange; HIV+ diabetic, gold; HIV- diabetic; blue). Cell types are broadly categorized as macrophage, monocyte, dendritic, or cycling and are ordered by proportion. The horizontal line represents the median proportion and the box depicts the lower and upper quartile limits. The whiskers are 1.5x the interquartile range. **f**, Differentially expressed genes in macrophages comparing diabetic persons with HIV (reference) with non-diabetic persons with HIV plotted as $\log_2$ fold change (x-axis) vs negative $\log_{10}$ FDR-adjusted p-value (y-axis). Genes with higher expression in diabetic persons with HIV are colored red while genes with lower

expression are colored blue. Abbreviations: cMo, classical monocytes; cDC1, conventional dendritic cell type 1; cDC2B, conventional dendritic cell type 2B; DC, dendritic cell; LAM, lipid-associated macrophage; Mac, macrophage; Mo, monocyte; PVM, perivascular macrophage; pDC, plasmacytoid dendritic cell

Figure 3. CD4 and CD8 T Effector Memory Proportion Increases with Glucose Intolerance in Persons with HIV. a, Uniform Manifold Approximation and Projection (UMAP) of T cells, natural killer cells, and innate lymphoid cells (n = 31,140 cells) from 91 individuals after subsetting and reclustering showing 16 distinct cell types/states. **b**, Dot plot showing selected gene markers on the x-axis and cell type on the y-axis. The dot size reflects the percentage of cells expressing the gene while the color reflects the scaled average expression. **c**, UMAP with CITE-seq surface antibodies for CD4, CD8, CD57, CD45RA, CD27, and CD16. **d**, Boxplot showing the proportion of each cell type as a percent of total lymphoid cells split by disease state (HIV+ non-diabetic, red; HIV+ prediabetic, orange; HIV+ diabetic, gold; HIV- diabetic; blue). Cell types are broadly categorized as T cells, natural killer cells, cycling, MAIT, gamma delta, and innate lymphoid cells and are ordered by proportion. The horizontal line represents the median proportion and the box depicts the lower and upper quartile limits. The whiskers are 1.5x the interquartile range. **e**, Spearman's correlation between $CD4^+$ T_{EM} cells and lipid associated macrophages with $CD4^+$ T_{EM} cells plotted on the x-axis (as a percentage of total $CD4^+$ T cells) and lipid associated macrophages plotted on the y-axis (as a percentage of total myeloid) for both HIV+ (left) and diabetic (right) persons. **f**, Spearman's correlation between $CD8^+$ T_{EM} cells and lipid associated macrophages with $CD8^+$ T_{EM} cells plotted on the x-axis (as a percentage of total $CD8^+$ T cells) and lipid associated macrophages plotted on the y-axis (as a percentage of total

myeloid) for both HIV+ (left) and diabetic (right) persons. Abbreviations: ILC, innate lymphoid cells; mNK, mature natural killer; NK, natural killer; TCM, T central memory; TEM, T effector memory; TEMRA, T effector memory RA+

Figure 4. Lipid Associated Macrophages are Associated with Higher Proportion of Myofibroblasts. a, Uniform Manifold Approximation and Projection (UMAP) of stromal cells (n = 87,674) from 91 individuals after subsetting and reclustering. **b**, Dot plot of stromal cells showing selected gene markers on the x axis and cell type on the y axis. The dot size reflects the percentage of cells expressing the gene while the color reflects the scaled average expression. **c**, Boxplot showing the proportion of each cell type as a percent of total stromal cells split by disease state (HIV+ non-diabetic, red; HIV+ prediabetic, orange; HIV+ diabetic, gold; HIV- diabetic; blue). The horizontal line represents the median proportion and the box depicts the lower and upper quartile limits. The whiskers are 1.5x the interquartile range. **d**, Scatter plot with lipid-associated macrophages (as a percent of total myeloid) on the x axis and myofibroblast (as a percent of total stromal) on the y-axis. The Spearman's correlation for all participants is significant ($p = 0.72$, $p < 0.001$). A regression line was added to the scatter plot split by disease state (HIV+ non-diabetic, red; HIV+ prediabetic, orange; HIV+ diabetic, gold; HIV- diabetic; blue). **e**, Scatter plot with $CD4^+$ effector memory cells (as a percent of total $CD4^+$ T cells) on the x axis and myofibroblast (as a percent of total stromal) for HIV+ (left) split by disease state (HIV+ non-diabetic, red; HIV+ prediabetic, orange; HIV+ diabetic, gold) and diabetics (right) split by HIV serostatus (HIV+ diabetic, gold; HIV- diabetic, blue). **f**, Scatter plot with $CD8^+$ effector memory cells (as a percent of total $CD8^+$ T cells) on the x axis and myofibroblast (as a percent of total stromal) for HIV+ (left) split by disease state (HIV+ non-diabetic, red; HIV+

prediabetic, orange; HIV+ diabetic, gold) and diabetics (right) split by HIV serostatus (HIV+ diabetic, gold; HIV- diabetic, blue). Abbreviations: ASC, Adipose Stem Cell; ECM, extracellular matrix

Supplemental Figures

Supplemental Figure 1. Bioinformatic Pipeline and Quality Metrics. a, Flow diagram of bioinformatic pipeline split into three sections: Homotypic doublet identification, heterotypic doublet identification, and integration and downstream processing. The Illumina NovaSeq 6000 Bcl files were demultiplexed into raw fastq files. Fastq files were aligned to the Human Genome Reference Consortium Build 38 (hg38) and cells were called using the Cell Ranger count function with default settings. Soupx was used to remove ambient RNA and the corrected count matrices were used to create a Seurat object. Simultaneously, Souporcell was used to genetically demultiplex the samples. Doublets identified by Souporcell were removed. Next, each Seurat object underwent quality control filtering and downstream dimensional reduction and clustering. Clusters were visually inspected and labeled as transcriptional doublets based on co-expression of major cell types and/or consisting of many doublets identified by DoubletFinder. The processed objects were then integrated using Harmony correction on the principal components prior to clustering. Cells were subclustered based on major cell lineages and transcriptional doublets were iteratively removed prior to reintegration. **b,** Barplot graph showing each lane (x-axis) and number of cells (y-axis). The graph is split by the total barcodes identified by Cell Ranger (red), the cells remaining after genetic demultiplexing and removal of homotypic doublets (green), and the cells remaining after applying quality control filters and removing transcriptional doublets (blue). **c,** Distribution of read counts per cell (y-axis) by lane (x-axis). **d,** Distribution of the number of features (genes) per cell (y-axis) by lane (x-axis). **e,** Example of

batch effect subclustering on T cells shown in a Uniform Manifold Approximation and Projection split by metabolic and HIV status: HIV+ non-diabetic (red), HIV+ prediabetic (orange), HIV+ diabetic (gold), HIV- diabetic (blue). After harmony correction, cells from each group are more uniformly distributed. **f,** Dot plot with selected genes on the x axis and cell type on the y axis. The size of the dot represents the percentage of cells with expression of that gene and the color of the dot represents the average expression level for that gene. **g,** Slingshot trajectory with capillary 2 as the root embedded on the UMAP (top) and Slingshot pseudotime (bottom). **h,** Scaled gene expressed ordered by pseudotime.

Supplemental Figure 2. Myeloid Cluster. a, Uniform Manifold Projection and Approximation (UMAP) of myeloid cells after downstream analysis on harmony-corrected principal components grouped by metabolic and HIV status: HIV+ non-diabetic (red), HIV+ prediabetic (orange), HIV+ diabetic (gold), HIV- diabetic (blue). **b,** Heatmap of scaled gene expression of the top 10 genes defining each annotated cluster using model-based analysis of single cell transcriptomics (MAST). **c,** UMAP with CITE-seq surface antibodies for CD14 (classical monocytes), CD16 (non-classical monocytes), CD1C (dendritic cells), CD11C (lipid associated macrophages). **d,** Scatter plot with lipid-associated macrophage as a percentage of total myeloid on the x-axis and classical monocytes as a percent of total myeloid on the y-axis showing significant inverse correlation by Spearman's test ($r = -0.71$, $p < 0.001$) . **e,** UMAP of myeloid cells with superimposed intermediate macrophage score on the current dataset (left) and Hildreth *et. al.* dataset (right). The score was derived using the AddModuleScore function implemented in Seurat by taking genes expressed > 2 fold in the intermediate macrophage population from Hildreth *et. al*. **f,** Seurat reference-based label transfer from the current study to Hildreth *et. al.*

(Hildreth *et. al.*, 2021). Abbreviations: cMo, classical monocyte; cDC1, conventional dendritic cell type 1; cDC2B, conventional dendritic cell type 2B; DC, dendritic cell; IM, intermediate macrophage; LAM, lipid-associated macrophage; Mac, macrophage; Mo, monocyte; nMo, non-classical macrophage; PVM, perivascular macrophage; pDC, plasmacytoid dendritic cell

Supplemental Figure 3. T and NK Cells. a, Heatmap of scaled gene expression of the top 10 genes defining each annotated cluster using model-based analysis of single cell transcriptomics (MAST). **b,** Uniform Manifold Approximation and Projection (UMAP) of $CD4^+$ T cells (n = 8,045 cells) subset from all T cells. **c,** Dot plot of $CD4^+$ T cells with selected genes on the x axis and cell type on the y axis. The size of the dot represents the percentage of cells with expression of that gene and the color of the dot represents the average expression level for that gene. **d,** Violin plots for CITE-seq expression of CD45RA, CD27, and CD57 with annotated cluster on the x-axis and expression level on the y-axis for $CD4^+$ T cells. **e,** Boxplot showing the proportion of each $CD4^+$ T cell type as a percent of total $CD4^+$ T cells split by disease state (HIV+ non-diabetic, red; HIV+ prediabetic, orange; HIV+ diabetic, gold; HIV- diabetic; blue). The horizontal line represents the median proportion and the box depicts the lower and upper quartile limits. The whiskers are 1.5x the interquartile range. **f,** UMAP of $CD8^+$ T cells (n = 11,325 cells) subset from all T cells. **g,** Dot plot of $CD8^+$ T cells with selected genes on the x axis and cell type on the y axis. The size of the dot represents the percentage of cells with expression of that gene and the color of the dot represents the average expression level for that gene. **h,** Violin plots for CITE-seq expression of CD45RA, CD27, and CD57 with annotated cluster on the x-axis and expression level on the y-axis for $CD8^+$ T cells. **i,** Boxplot showing the proportion of each $CD8^+$ T cell type as a percent of total $CD8^+$ T cells split by disease state (HIV+ non-diabetic, red;

HIV+ prediabetic, orange; HIV+ diabetic, gold; HIV- diabetic; blue). The horizontal line represents the median proportion and the box depicts the lower and upper quartile limits. The whiskers are 1.5x the interquartile range. Abbreviations: ILC, innate lymphoid cells; mNK, mature natural killer; NK, natural killer; TCM, T central memory; TEM, T effector memory, TEMRA, T effector memory RA^+

Supplemental Figure 4. Fibro-Adipogenic Cells. a, Heatmap of scaled gene expression of the top 10 genes defining each annotated stromal cluster using model-based analysis of single cell transcriptomics (MAST). **b,** Violin plot of scaled expression of *CFD, DCN, LUM, MGP, PI16, GSN, and FBLN1* that are markers of progenitor cells (y axis) by cluster (x axis) and scaled expression of *CXCL14, COL4A1, ZFP36, MYC, JUN, FOS, CEBPD, PPARG, FABP4, C7, LPL, and CIDEC* that are markers of preadipocytes (y axis) by cluster (x axis). **c,** Gene Ontology (GO) over-representation analysis with preadipocyte cluster on the x-axis and GO pathway and the y-axis. The size of the circle denotes the negative $\log_{10}$ p-value while the color denotes the number of genes assigned to the pathway. **d,** Scaled module score using gene markers that identify CD142+ (top left), ICAM+ (top right), and DPP4 (bottom left) clusters from Merrick *et. al.* superimposed on the fibro-adipogenic UMAP. **e,** Scaled module score using gene markers that identify P1 (top left), P2 (top right), and P3 (bottom left) clusters from Schwalie *et. al.* superimposed on the fibro-adipogenic UMAP. **f,** Scaled module scoring using gene markers that identify FAP1 (top left), FAP2 (top right), FAP3 (bottom left), and FAP4 (bottom right) clusters from Sarvari *et. al.* superimposed on the fibro-adipogenic UMAP.

References

Abana, C.O., Pilkinton, M.A., Gaudieri, S., Chopra, A., McDonnell, W.J., Wanjalla, C., Barnett, L., Gangula, R., Hager, C., Jung, D.K., *et al.* (2017). Cytomegalovirus (CMV) Epitope-Specific CD4(+) T Cells Are Inflated in HIV(+) CMV(+) Subjects. J Immunol *199*, 3187-3201.

Acosta, J.R., Joost, S., Karlsson, K., Ehrlund, A., Li, X., Aouadi, M., Kasper, M., Arner, P., Ryden, M., and Laurencikiene, J. (2017). Single cell transcriptomics suggest that human adipocyte progenitor cells constitute a homogeneous cell population. Stem Cell Res Ther *8*, 250.

Alexander, R.W., and Harrell, D.B. (2013). Autologous fat grafting: use of closed syringe microcannula system for enhanced autologous structural grafting. Clin Cosmet Investig Dermatol *6*, 91-102.

Amano, S.U., Cohen, J.L., Vangala, P., Tencerova, M., Nicoloro, S.M., Yawe, J.C., Shen, Y., Czech, M.P., and Aouadi, M. (2014). Local proliferation of macrophages contributes to obesity-associated adipose tissue inflammation. Cell Metab *19*, 162-171.

American Diabetes, A. (2020). 2. Classification and Diagnosis of Diabetes: Standards of Medical Care in Diabetes-2020. Diabetes Care *43*, S14-S31.

Angueira, A.R., Sakers, A.P., Holman, C.D., Cheng, L., Arbocco, M.N., Shamsi, F., Lynes, M.D., Shrestha, R., Okada, C., Batmanov, K., *et al.* (2021). Defining the lineage of thermogenic perivascular adipose tissue. Nat Metab *3*, 469-484.

Appay, V., and Sauce, D. (2008). Immune activation and inflammation in HIV-1 infection: causes and consequences. J Pathol *214*, 231-241.

Bofill, M., Mocroft, A., Lipman, M., Medina, E., Borthwick, N.J., Sabin, C.A., Timms, A., Winter, M., Baptista, L., Johnson, M.A., *et al.* (1996). Increased numbers of primed activated

CD8+CD38+CD45RO+ T cells predict the decline of CD4+ T cells in HIV-1-infected patients. AIDS *10*, 827-834.

Boulenouar, S., Michelet, X., Duquette, D., Alvarez, D., Hogan, A.E., Dold, C., O'Connor, D., Stutte, S., Tavakkoli, A., Winters, D., *et al.* (2017). Adipose Type One Innate Lymphoid Cells Regulate Macrophage Homeostasis through Targeted Cytotoxicity. Immunity *46*, 273-286.

Brahma, P.K., Zhang, H., Murray, B.S., Shu, F.J., Sidell, N., Seli, E., and Kallen, C.B. (2012). The mRNA-binding protein Zfp36 is upregulated by beta-adrenergic stimulation and represses IL-6 production in 3T3-L1 adipocytes. Obesity (Silver Spring) *20*, 40-47.

Brestoff, J.R., Kim, B.S., Saenz, S.A., Stine, R.R., Monticelli, L.A., Sonnenberg, G.F., Thome, J.J., Farber, D.L., Lutfy, K., Seale, P., and Artis, D. (2015). Group 2 innate lymphoid cells promote beiging of white adipose tissue and limit obesity. Nature *519*, 242-246.

Brestoff, J.R., Wilen, C.B., Moley, J.R., Li, Y., Zou, W., Malvin, N.P., Rowen, M.N., Saunders, B.T., Ma, H., Mack, M.R., *et al.* (2021). Intercellular Mitochondria Transfer to Macrophages Regulates White Adipose Tissue Homeostasis and Is Impaired in Obesity. Cell Metab *33*, 270-282 e278.

Brown, C.C., Gudjonson, H., Pritykin, Y., Deep, D., Lavallee, V.P., Mendoza, A., Fromme, R., Mazutis, L., Ariyan, C., Leslie, C., *et al.* (2019). Transcriptional Basis of Mouse and Human Dendritic Cell Heterogeneity. Cell *179*, 846-863 e824.

Burl, R.B., Ramseyer, V.D., Rondini, E.A., Pique-Regi, R., Lee, Y.H., and Granneman, J.G. (2018). Deconstructing Adipogenesis Induced by beta3-Adrenergic Receptor Activation with Single-Cell Expression Profiling. Cell Metab *28*, 300-309 e304.

Caso, G., McNurlan, M.A., Mileva, I., Zemlyak, A., Mynarcik, D.C., and Gelato, M.C. (2013). Peripheral fat loss and decline in adipogenesis in older humans. Metabolism *62*, 337-340.

Chakarov, S., Lim, H.Y., Tan, L., Lim, S.Y., See, P., Lum, J., Zhang, X.M., Foo, S., Nakamizo, S., Duan, K., *et al.* (2019). Two distinct interstitial macrophage populations coexist across tissues in specific subtissular niches. Science *363*.

Chang, E., Varghese, M., and Singer, K. (2018). Gender and Sex Differences in Adipose Tissue. Curr Diab Rep *18*, 69.

Cho, K.W., Morris, D.L., DelProposto, J.L., Geletka, L., Zamarron, B., Martinez-Santibanez, G., Meyer, K.A., Singer, K., O'Rourke, R.W., and Lumeng, C.N. (2014). An MHC II-dependent activation loop between adipose tissue macrophages and CD4+ T cells controls obesity-induced inflammation. Cell Rep *9*, 605-617.

Cinti, S., Mitchell, G., Barbatelli, G., Murano, I., Ceresi, E., Faloia, E., Wang, S., Fortier, M., Greenberg, A.S., and Obin, M.S. (2005). Adipocyte death defines macrophage localization and function in adipose tissue of obese mice and humans. J Lipid Res *46*, 2347-2355.

Cipolletta, D., Feuerer, M., Li, A., Kamei, N., Lee, J., Shoelson, S.E., Benoist, C., and Mathis, D. (2012). PPAR-gamma is a major driver of the accumulation and phenotype of adipose tissue Treg cells. Nature *486*, 549-553.

Couturier, J., Suliburk, J.W., Brown, J.M., Luke, D.J., Agarwal, N., Yu, X., Nguyen, C., Iyer, D., Kozinetz, C.A., Overbeek, P.A., *et al.* (2015). Human adipose tissue as a reservoir for memory CD4+ T cells and HIV. AIDS *29*, 667-674.

Damouche, A., Lazure, T., Avettand-Fenoel, V., Huot, N., Dejucq-Rainsford, N., Satie, A.P., Melard, A., David, L., Gommet, C., Ghosn, J., *et al.* (2015). Adipose Tissue Is a Neglected Viral Reservoir and an Inflammatory Site during Chronic HIV and SIV Infection. PLoS Pathog *11*, e1005153.

Day, C.L., Kaufmann, D.E., Kiepiela, P., Brown, J.A., Moodley, E.S., Reddy, S., Mackey, E.W., Miller, J.D., Leslie, A.J., DePierres, C., *et al.* (2006). PD-1 expression on HIV-specific T cells is associated with T-cell exhaustion and disease progression. Nature *443*, 350-354.

Deiuliis, J., Shah, Z., Shah, N., Needleman, B., Mikami, D., Narula, V., Perry, K., Hazey, J., Kampfrath, T., Kollengode, M., *et al.* (2011). Visceral adipose inflammation in obesity is associated with critical alterations in tregulatory cell numbers. PLoS One *6*, e16376.

Dutertre, C.A., Becht, E., Irac, S.E., Khalilnezhad, A., Narang, V., Khalilnezhad, S., Ng, P.Y., van den Hoogen, L.L., Leong, J.Y., Lee, B., *et al.* (2019). Single-Cell Analysis of Human Mononuclear Phagocytes Reveals Subset-Defining Markers and Identifies Circulating Inflammatory Dendritic Cells. Immunity *51*, 573-589 e578.

Emont, M.P., Jacobs, C., Essene, A.L., Pant, D., Tenen, D., Colleluori, G., Di Vincenzo, A., Jorgensen, A.M., Dashti, H., Stefek, A., *et al.* (2022). A single-cell atlas of human and mouse white adipose tissue. Nature.

Fabbrini, E., Cella, M., McCartney, S.A., Fuchs, A., Abumrad, N.A., Pietka, T.A., Chen, Z., Finck, B.N., Han, D.H., Magkos, F., *et al.* (2013). Association between specific adipose tissue CD4+ T-cell populations and insulin resistance in obese individuals. Gastroenterology *145*, 366-374 e361-363.

Feuerer, M., Herrero, L., Cipolletta, D., Naaz, A., Wong, J., Nayer, A., Lee, J., Goldfine, A.B., Benoist, C., Shoelson, S., and Mathis, D. (2009). Lean, but not obese, fat is enriched for a unique population of regulatory T cells that affect metabolic parameters. Nat Med *15*, 930-939.

Finak, G., McDavid, A., Yajima, M., Deng, J., Gersuk, V., Shalek, A.K., Slichter, C.K., Miller, H.W., McElrath, M.J., Prlic, M., *et al.* (2015). MAST: a flexible statistical framework for

assessing transcriptional changes and characterizing heterogeneity in single-cell RNA sequencing data. Genome Biol *16*, 278.

Fuchs, A., Samovski, D., Smith, G.I., Cifarelli, V., Farabi, S.S., Yoshino, J., Pietka, T., Chang, S.W., Ghosh, S., Myckatyn, T.M., and Klein, S. (2021). Associations Among Adipose Tissue Immunology, Inflammation, Exosomes and Insulin Sensitivity in People With Obesity and Nonalcoholic Fatty Liver Disease. Gastroenterology *161*, 968-981 e912.

Gabriel, C.L., Ye, F., Fan, R., Nair, S., Terry, J.G., Carr, J.J., Silver, H., Baker, P., Hannah, L., Wanjalla, C., *et al.* (2021). Hepatic Steatosis and Ectopic Fat Are Associated With Differences in Subcutaneous Adipose Tissue Gene Expression in People With HIV. Hepatol Commun *5*, 1224-1237.

Ghaben, A.L., and Scherer, P.E. (2019). Adipogenesis and metabolic health. Nat Rev Mol Cell Biol *20*, 242-258.

Goldberg, E.L., Shchukina, I., Asher, J.L., Sidorov, S., Artyomov, M.N., and Dixit, V.D. (2020). Ketogenesis activates metabolically protective gammadelta T cells in visceral adipose tissue. Nat Metab *2*, 50-61.

Gu, Z., Eils, R., and Schlesner, M. (2016). Complex heatmaps reveal patterns and correlations in multidimensional genomic data. Bioinformatics *32*, 2847-2849.

Hafemeister, C., and Satija, R. (2019). Normalization and variance stabilization of single-cell RNA-seq data using regularized negative binomial regression. Genome Biol *20*, 296.

Halberg, N., Khan, T., Trujillo, M.E., Wernstedt-Asterholm, I., Attie, A.D., Sherwani, S., Wang, Z.V., Landskroner-Eiger, S., Dineen, S., Magalang, U.J., *et al.* (2009). Hypoxia-inducible factor 1alpha induces fibrosis and insulin resistance in white adipose tissue. Mol Cell Biol *29*, 4467-4483.

Hao, Y., Hao, S., Andersen-Nissen, E., Mauck, W.M., 3rd, Zheng, S., Butler, A., Lee, M.J., Wilk, A.J., Darby, C., Zager, M., *et al.* (2021). Integrated analysis of multimodal single-cell data. Cell *184*, 3573-3587 e3529.

Hazenberg, M.D., Hamann, D., Schuitemaker, H., and Miedema, F. (2000). T cell depletion in HIV-1 infection: how CD4+ T cells go out of stock. Nat Immunol *1*, 285-289.

Heaton, H., Talman, A.M., Knights, A., Imaz, M., Gaffney, D.J., Durbin, R., Hemberg, M., and Lawniczak, M.K.N. (2020). Souporcell: robust clustering of single-cell RNA-seq data by genotype without reference genotypes. Nat Methods *17*, 615-620.

Herrin, M., Tate, J.P., Akgun, K.M., Butt, A.A., Crothers, K., Freiberg, M.S., Gibert, C.L., Leaf, D.A., Rimland, D., Rodriguez-Barradas, M.C., *et al.* (2016). Weight Gain and Incident Diabetes Among HIV-Infected Veterans Initiating Antiretroviral Therapy Compared With Uninfected Individuals. J Acquir Immune Defic Syndr *73*, 228-236.

Hildreth, A.D., Ma, F., Wong, Y.Y., Sun, R., Pellegrini, M., and O'Sullivan, T.E. (2021). Single-cell sequencing of human white adipose tissue identifies new cell states in health and obesity. Nat Immunol *22*, 639-653.

Hill, D.A., Lim, H.W., Kim, Y.H., Ho, W.Y., Foong, Y.H., Nelson, V.L., Nguyen, H.C.B., Chegireddy, K., Kim, J., Habertheuer, A., *et al.* (2018). Distinct macrophage populations direct inflammatory versus physiological changes in adipose tissue. Proc Natl Acad Sci U S A *115*, E5096-E5105.

Hu, Z., Liu, W., Hua, X., Chen, X., Chang, Y., Hu, Y., Xu, Z., and Song, J. (2021). Single-Cell Transcriptomic Atlas of Different Human Cardiac Arteries Identifies Cell Types Associated With Vascular Physiology. Arterioscler Thromb Vasc Biol *41*, 1408-1427.

Huang, Z., Chen, B., Liu, X., Li, H., Xie, L., Gao, Y., Duan, R., Li, Z., Zhang, J., Zheng, Y., and Su, W. (2021). Effects of sex and aging on the immune cell landscape as assessed by single-cell transcriptomic analysis. Proc Natl Acad Sci U S A *118*.

Jaacks, L.M., Vandevijvere, S., Pan, A., McGowan, C.J., Wallace, C., Imamura, F., Mozaffarian, D., Swinburn, B., and Ezzati, M. (2019). The obesity transition: stages of the global epidemic. Lancet Diabetes Endocrinol *7*, 231-240.

Jaitin, D.A., Adlung, L., Thaiss, C.A., Weiner, A., Li, B., Descamps, H., Lundgren, P., Bleriot, C., Liu, Z., Deczkowska, A., *et al.* (2019). Lipid-Associated Macrophages Control Metabolic Homeostasis in a Trem2-Dependent Manner. Cell *178*, 686-698 e614.

Jan, V., Cervera, P., Maachi, M., Baudrimont, M., Kim, M., Vidal, H., Girard, P.M., Levan, P., Rozenbaum, W., Lombes, A., *et al.* (2004). Altered fat differentiation and adipocytokine expression are inter-related and linked to morphological changes and insulin resistance in HIV-1-infected lipodystrophic patients. Antivir Ther *9*, 555-564.

Kahn, C.R., Wang, G., and Lee, K.Y. (2019). Altered adipose tissue and adipocyte function in the pathogenesis of metabolic syndrome. J Clin Invest *129*, 3990-4000.

Kohlgruber, A.C., Gal-Oz, S.T., LaMarche, N.M., Shimazaki, M., Duquette, D., Koay, H.F., Nguyen, H.N., Mina, A.I., Paras, T., Tavakkoli, A., *et al.* (2018). gammadelta T cells producing interleukin-17A regulate adipose regulatory T cell homeostasis and thermogenesis. Nat Immunol *19*, 464-474.

Korsunsky, I., Millard, N., Fan, J., Slowikowski, K., Zhang, F., Wei, K., Baglaenko, Y., Brenner, M., Loh, P.R., and Raychaudhuri, S. (2019). Fast, sensitive and accurate integration of single-cell data with Harmony. Nat Methods *16*, 1289-1296.

Kratz, M., Coats, B.R., Hisert, K.B., Hagman, D., Mutskov, V., Peris, E., Schoenfelt, K.Q., Kuzma, J.N., Larson, I., Billing, P.S., *et al.* (2014). Metabolic dysfunction drives a mechanistically distinct proinflammatory phenotype in adipose tissue macrophages. Cell Metab *20*, 614-625.

Lee, B.C., Kim, M.S., Pae, M., Yamamoto, Y., Eberle, D., Shimada, T., Kamei, N., Park, H.S., Sasorith, S., Woo, J.R., *et al.* (2016). Adipose Natural Killer Cells Regulate Adipose Tissue Macrophages to Promote Insulin Resistance in Obesity. Cell Metab *23*, 685-698.

Lee, J.E., Schmidt, H., Lai, B., and Ge, K. (2019). Transcriptional and Epigenomic Regulation of Adipogenesis. Mol Cell Biol *39*.

Lui, Q., Shepherd, B., and Li, C. (2020). PResiduals: An R package for residual analysis using probability-scale residuals. Jounral of Statistical Software *94*, 1-27.

Lumeng, C.N., Bodzin, J.L., and Saltiel, A.R. (2007a). Obesity induces a phenotypic switch in adipose tissue macrophage polarization. J Clin Invest *117*, 175-184.

Lumeng, C.N., Deyoung, S.M., and Saltiel, A.R. (2007b). Macrophages block insulin action in adipocytes by altering expression of signaling and glucose transport proteins. Am J Physiol Endocrinol Metab *292*, E166-174.

Macdougall, C.E., Wood, E.G., Loschko, J., Scagliotti, V., Cassidy, F.C., Robinson, M.E., Feldhahn, N., Castellano, L., Voisin, M.B., Marelli-Berg, F., *et al.* (2018). Visceral Adipose Tissue Immune Homeostasis Is Regulated by the Crosstalk between Adipocytes and Dendritic Cell Subsets. Cell Metab *27*, 588-601 e584.

Marcelin, G., Ferreira, A., Liu, Y., Atlan, M., Aron-Wisnewsky, J., Pelloux, V., Botbol, Y., Ambrosini, M., Fradet, M., Rouault, C., *et al.* (2017). A PDGFRalpha-Mediated Switch toward

CD9(high) Adipocyte Progenitors Controls Obesity-Induced Adipose Tissue Fibrosis. Cell Metab *25*, 673-685.

McGinnis, C.S., Murrow, L.M., and Gartner, Z.J. (2019). DoubletFinder: Doublet Detection in Single-Cell RNA Sequencing Data Using Artificial Nearest Neighbors. Cell Syst *8*, 329-337 e324.

Merrick, D., Sakers, A., Irgebay, Z., Okada, C., Calvert, C., Morley, M.P., Percec, I., and Seale, P. (2019). Identification of a mesenchymal progenitor cell hierarchy in adipose tissue. Science *364*.

Min, S.Y., Desai, A., Yang, Z., Sharma, A., DeSouza, T., Genga, R.M.J., Kucukural, A., Lifshitz, L.M., Nielsen, S., Scheele, C., *et al.* (2019). Diverse repertoire of human adipocyte subtypes develops from transcriptionally distinct mesenchymal progenitor cells. Proc Natl Acad Sci U S A *116*, 17970-17979.

Morris, D.L., Cho, K.W., Delproposto, J.L., Oatmen, K.E., Geletka, L.M., Martinez-Santibanez, G., Singer, K., and Lumeng, C.N. (2013). Adipose tissue macrophages function as antigen-presenting cells and regulate adipose tissue CD4+ T cells in mice. Diabetes *62*, 2762-2772.

Muhl, L., Genove, G., Leptidis, S., Liu, J., He, L., Mocci, G., Sun, Y., Gustafsson, S., Buyandelger, B., Chivukula, I.V., *et al.* (2020). Single-cell analysis uncovers fibroblast heterogeneity and criteria for fibroblast and mural cell identification and discrimination. Nat Commun *11*, 3953.

Nansseu, J.R., Bigna, J.J., Kaze, A.D., and Noubiap, J.J. (2018). Incidence and Risk Factors for Prediabetes and Diabetes Mellitus Among HIV-infected Adults on Antiretroviral Therapy: A Systematic Review and Meta-analysis. Epidemiology *29*, 431-441.

Neuhaus, J., Jacobs, D.R., Jr., Baker, J.V., Calmy, A., Duprez, D., La Rosa, A., Kuller, L.H., Pett, S.L., Ristola, M., Ross, M.J., *et al.* (2010). Markers of inflammation, coagulation, and renal function are elevated in adults with HIV infection. J Infect Dis *201*, 1788-1795.

Nishimura, S., Manabe, I., Nagasaki, M., Eto, K., Yamashita, H., Ohsugi, M., Otsu, M., Hara, K., Ueki, K., Sugiura, S., *et al.* (2009). CD8+ effector T cells contribute to macrophage recruitment and adipose tissue inflammation in obesity. Nat Med *15*, 914-920.

Oguri, Y., Shinoda, K., Kim, H., Alba, D.L., Bolus, W.R., Wang, Q., Brown, Z., Pradhan, R.N., Tajima, K., Yoneshiro, T., *et al.* (2020). CD81 Controls Beige Fat Progenitor Cell Growth and Energy Balance via FAK Signaling. Cell *182*, 563-577 e520.

Ouyang, J.F., Kamaraj, U.S., Cao, E.Y., and Rackham, O.J.L. (2021). ShinyCell: Simple and sharable visualisation of single-cell gene expression data. Bioinformatics.

Patsouris, D., Li, P.P., Thapar, D., Chapman, J., Olefsky, J.M., and Neels, J.G. (2008). Ablation of CD11c-positive cells normalizes insulin sensitivity in obese insulin resistant animals. Cell Metab *8*, 301-309.

Piera-Velazquez, S., and Jimenez, S.A. (2019). Endothelial to Mesenchymal Transition: Role in Physiology and in the Pathogenesis of Human Diseases. Physiol Rev *99*, 1281-1324.

Russo, L., and Lumeng, C.N. (2018). Properties and functions of adipose tissue macrophages in obesity. Immunology *155*, 407-417.

Saeedi, P., Petersohn, I., Salpea, P., Malanda, B., Karuranga, S., Unwin, N., Colagiuri, S., Guariguata, L., Motala, A.A., Ogurtsova, K., *et al.* (2019). Global and regional diabetes prevalence estimates for 2019 and projections for 2030 and 2045: Results from the International Diabetes Federation Diabetes Atlas, 9(th) edition. Diabetes Res Clin Pract *157*, 107843.

Sarvari, A.K., Van Hauwaert, E.L., Markussen, L.K., Gammelmark, E., Marcher, A.B., Ebbesen, M.F., Nielsen, R., Brewer, J.R., Madsen, J.G.S., and Mandrup, S. (2021). Plasticity of Epididymal Adipose Tissue in Response to Diet-Induced Obesity at Single-Nucleus Resolution. Cell Metab *33*, 437-453 e435.

Sathaliyawala, T., Kubota, M., Yudanin, N., Turner, D., Camp, P., Thome, J.J., Bickham, K.L., Lerner, H., Goldstein, M., Sykes, M., *et al.* (2013). Distribution and compartmentalization of human circulating and tissue-resident memory T cell subsets. Immunity *38*, 187-197.

Schupp, J.C., Adams, T.S., Cosme, C., Jr., Raredon, M.S.B., Yuan, Y., Omote, N., Poli, S., Chioccioli, M., Rose, K.A., Manning, E.P., *et al.* (2021). Integrated Single-Cell Atlas of Endothelial Cells of the Human Lung. Circulation *144*, 286-302.

Schwalie, P.C., Dong, H., Zachara, M., Russeil, J., Alpern, D., Akchiche, N., Caprara, C., Sun, W., Schlaudraff, K.U., Soldati, G., *et al.* (2018). A stromal cell population that inhibits adipogenesis in mammalian fat depots. Nature *559*, 103-108.

Shah, A.S.V., Stelzle, D., Lee, K.K., Beck, E.J., Alam, S., Clifford, S., Longenecker, C.T., Strachan, F., Bagchi, S., Whiteley, W., *et al.* (2018). Global Burden of Atherosclerotic Cardiovascular Disease in People Living With HIV: Systematic Review and Meta-Analysis. Circulation *138*, 1100-1112.

Shikuma, C.M., Gangcuangco, L.M., Killebrew, D.A., Libutti, D.E., Chow, D.C., Nakamoto, B.K., Liang, C.Y., Milne, C.I., Ndhlovu, L.C., Barbour, J.D., *et al.* (2014). The role of HIV and monocytes/macrophages in adipose tissue biology. J Acquir Immune Defic Syndr *65*, 151-159.

Stoeckius, M., Hafemeister, C., Stephenson, W., Houck-Loomis, B., Chattopadhyay, P.K., Swerdlow, H., Satija, R., and Smibert, P. (2017). Simultaneous epitope and transcriptome measurement in single cells. Nat Methods *14*, 865-868.

Stoeckius, M., Zheng, S., Houck-Loomis, B., Hao, S., Yeung, B.Z., Mauck, W.M., 3rd, Smibert, P., and Satija, R. (2018). Cell Hashing with barcoded antibodies enables multiplexing and doublet detection for single cell genomics. Genome Biol *19*, 224.

Street, K., Risso, D., Fletcher, R.B., Das, D., Ngai, J., Yosef, N., Purdom, E., and Dudoit, S. (2018). Slingshot: cell lineage and pseudotime inference for single-cell transcriptomics. BMC Genomics *19*, 477.

Stuart, T., Butler, A., Hoffman, P., Hafemeister, C., Papalexi, E., Mauck, W.M., 3rd, Hao, Y., Stoeckius, M., Smibert, P., and Satija, R. (2019). Comprehensive Integration of Single-Cell Data. Cell *177*, 1888-1902 e1821.

Sun, K., Tordjman, J., Clement, K., and Scherer, P.E. (2013). Fibrosis and adipose tissue dysfunction. Cell Metab *18*, 470-477.

Sun, W., Dong, H., Balaz, M., Slyper, M., Drokhlyansky, E., Colleluori, G., Giordano, A., Kovanicova, Z., Stefanicka, P., Balazova, L., *et al.* (2020). snRNA-seq reveals a subpopulation of adipocytes that regulates thermogenesis. Nature *587*, 98-102.

Tabib, T., Huang, M., Morse, N., Papazoglou, A., Behera, R., Jia, M., Bulik, M., Monier, D.E., Benos, P.V., Chen, W., *et al.* (2021). Myofibroblast transcriptome indicates SFRP2(hi) fibroblast progenitors in systemic sclerosis skin. Nat Commun *12*, 4384.

Travaglini, K.J., Nabhan, A.N., Penland, L., Sinha, R., Gillich, A., Sit, R.V., Chang, S., Conley, S.D., Mori, Y., Seita, J., *et al.* (2020). A molecular cell atlas of the human lung from single-cell RNA sequencing. Nature *587*, 619-625.

Urs, S., Smith, C., Campbell, B., Saxton, A.M., Taylor, J., Zhang, B., Snoddy, J., Jones Voy, B., and Moustaid-Moussa, N. (2004). Gene expression profiling in human preadipocytes and adipocytes by microarray analysis. J Nutr *134*, 762-770.

Van den Berge, K., Roux de Bezieux, H., Street, K., Saelens, W., Cannoodt, R., Saeys, Y., Dudoit, S., and Clement, L. (2020). Trajectory-based differential expression analysis for single-cell sequencing data. Nat Commun *11*, 1201.

Vasanthakumar, A., Chisanga, D., Blume, J., Gloury, R., Britt, K., Henstridge, D.C., Zhan, Y., Torres, S.V., Liene, S., Collins, N., *et al.* (2020). Sex-specific adipose tissue imprinting of regulatory T cells. Nature *579*, 581-585.

Vijay, J., Gauthier, M.F., Biswell, R.L., Louiselle, D.A., Johnston, J.J., Cheung, W.A., Belden, B., Pramatarova, A., Biertho, L., Gibson, M., *et al.* (2020). Single-cell analysis of human adipose tissue identifies depot and disease specific cell types. Nat Metab *2*, 97-109.

Wanjalla, C.N., McDonnell, W.J., Barnett, L., Simmons, J.D., Furch, B.D., Lima, M.C., Woodward, B.O., Fan, R., Fei, Y., Baker, P.G., *et al.* (2019). Adipose Tissue in Persons With HIV Is Enriched for CD4(+) T Effector Memory and T Effector Memory RA(+) Cells, Which Show Higher CD69 Expression and CD57, CX3CR1, GPR56 Co-expression With Increasing Glucose Intolerance. Front Immunol *10*, 408.

Wanjalla, C.N., McDonnell, W.J., Ram, R., Chopra, A., Gangula, R., Leary, S., Mashayekhi, M., Simmons, J.D., Warren, C.M., Bailin, S., *et al.* (2021). Single-cell analysis shows that adipose tissue of persons with both HIV and diabetes is enriched for clonal, cytotoxic, and CMV-specific CD4+ T cells. Cell Rep Med *2*, 100205.

Winer, S., Chan, Y., Paltser, G., Truong, D., Tsui, H., Bahrami, J., Dorfman, R., Wang, Y., Zielenski, J., Mastronardi, F., *et al.* (2009). Normalization of obesity-associated insulin resistance through immunotherapy. Nat Med *15*, 921-929.

Young, M.D., and Behjati, S. (2020). SoupX removes ambient RNA contamination from droplet-based single-cell RNA sequencing data. Gigascience *9*.

Zicari, S., Sessa, L., Cotugno, N., Ruggiero, A., Morrocchi, E., Concato, C., Rocca, S., Zangari, P., Manno, E.C., and Palma, P. (2019). Immune Activation, Inflammation, and Non-AIDS Co-Morbidities in HIV-Infected Patients under Long-Term ART. Viruses *11*.

Table 1. Cohort Characteristics

	HIV+ non-diabetic (n = 20)	HIV+ prediabetic (n = 19)	HIV+ diabetic (n = 20)	HIV- diabetic (n = 32)	P value
Age (years)	46 (40, 52)	42 (38, 54)	55 (48, 62)	59 (51, 64)	P < 0.001
Race					
White	0.55 $^{11}/_{20}$	0.47 $^{9}/_{19}$	0.50 $^{10}/_{20}$	0.66 $^{21}/_{32}$	P = 0.84
Black	0.35 $^{7}/_{20}$	0.42 $^{8}/_{19}$	0.40 $^{8}/_{20}$	0.31 $^{10}/_{32}$	
Other	0.10 $^{2}/_{20}$	0.11 $^{2}/_{19}$	0.10 $^{2}/_{20}$	0.03 $^{1}/_{32}$	
Sex, Female	0.35 $^{7}/_{20}$	0.21 $^{4}/_{19}$	0.25 $^{5}/_{20}$	0.72 $^{23}/_{32}$	P < 0.001
Body mass index (kg/m^2)	31.0 (28.6, 34.7)	29.4 (28.4, 34.2)	33.2 (30.2, 37.8)	38.0 (33.0, 41.5)	P < 0.001
Metformin Use	0.00 $^{0}/_{20}$	0.00 $^{0}/_{19}$	0.60 $^{12}/_{20}$	0.44 $^{14}/_{32}$	P<0.001
HIV-specific data					
CD4 Count at Enrollment (cells/mm^3)	784 (660, 941)	684 (544, 1000)	893 (724, 1102)		P = 0.53
Exposure to Thymidine Analogue, Yes	0.26 $^{5}/_{19}$	0.11 $^{2}/_{19}$	0.22 $^{4}/_{18}$		P = 0.45
ART Regimen					
Integrase Inhibitor & NRTIs	0.55 $^{11}/_{20}$	0.53 $^{10}/_{19}$	0.50 $^{10}/_{20}$		P = 0.98
NNRTI & NRTIs	0.05 $^{1}/_{20}$	0.16 $^{3}/_{19}$	0.10 $^{2}/_{20}$		
Protease Inhibitor and NRTIs	0.20 $^{4}/_{20}$	0.16 $^{3}/_{19}$	0.20 $^{4}/_{20}$		
Integrase and Protease Inhibitor	0.10 $^{2}/_{20}$	0.05 $^{1}/_{19}$	0.05 $^{1}/_{20}$		
Other	0.10 $^{2}/_{20}$	0.11 $^{2}/_{19}$	0.15 $^{3}/_{20}$		

Continuous variables are shown as median value with interquartile range. Categorical variables are shown as proportion.

Abbreviations: ART, anti-retroviral therapy; HIV+, persons with HIV; HIV-, persons without HIV; NNRTI, non-nucleoside reverse transcriptase inhibitor; NRTI, nucleoside reverse transcriptase inhibitor

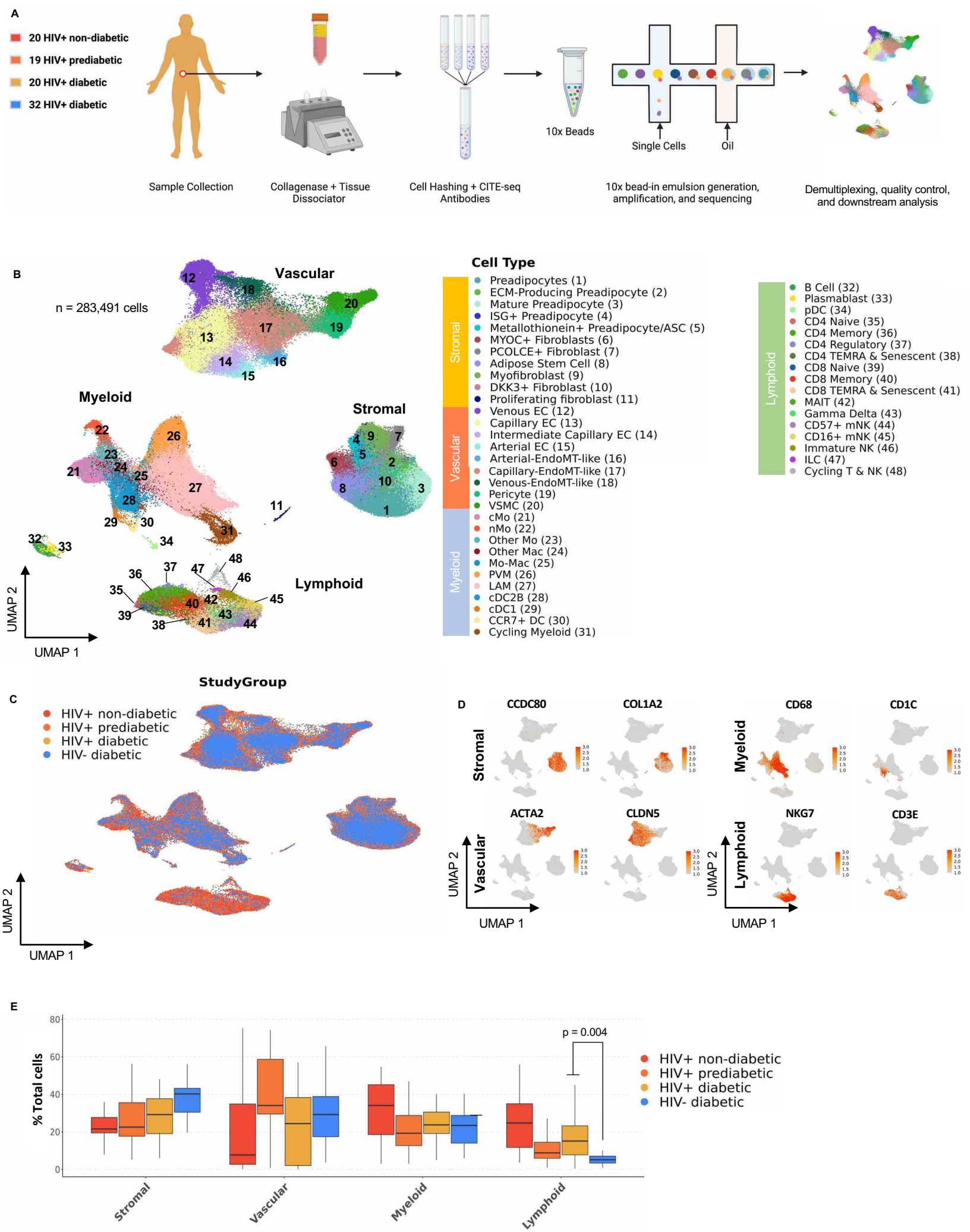
A
20 HIV+ non-diabetic
19 HIV+ prediabetic
20 HIV+ diabetic
32 HIV+ diabetic
10x Beads
Single Cells
Oil
Sample Collection
Collagenase + Tissue Dissociator
Cell Hashing + CITE-seq Antibodies
10x bead-in emulsion generation, amplification, and sequencing
Demultiplexing, quality control, and downstream analysis
B
n = 283,491 cells
Vascular
Myeloid
Stromal
Lymphoid
UMAP 2
UMAP 1
Cell Type
Stromal
Vascular
Myeloid
Lymphoid
Preadipocytes (1)
ECM-Producing Preadipocyte (2)
Mature Preadipocyte (3)
ISG+ Preadipocyte (4)
Metallothionein+ Preadipocyte/ASC (5)
MYOC+ Fibroblasts (6)
PCOLCE+ Fibroblast (7)
Adipose Stem Cell (8)
Myofibroblast (9)
DKK3+ Fibroblast (10)
Proliferating fibroblast (11)
Venous EC (12)
Capillary EC (13)
Intermediate Capillary EC (14)
Arterial EC (15)
Arterial-EndoMT-like (16)
Capillary-EndoMT-like (17)
Venous-EndoMT-like (18)
Pericyte (19)
VSMC (20)
cMo (21)
nMo (22)
Other Mo (23)
Other Mac (24)
Mo-Mac (25)
PVM (26)
LAM (27)
cDC2B (28)
cDC1 (29)
CCR7+ DC (30)
Cycling Myeloid (31)
B Cell (32)
Plasmablast (33)
pDC (34)
CD4 Naive (35)
CD4 Memory (36)
CD4 Regulatory (37)
CD4 TEMRA & Senescent (38)
CD8 Naive (39)
CD8 Memory (40)
CD8 TEMRA & Senescent (41)
MAIT (42)
Gamma Delta (43)
CD57+ mNK (44)
CD16+ mNK (45)
Immature NK (46)
ILC (47)
Cycling T & NK (48)
C
StudyGroup
HIV+ non-diabetic
HIV+ prediabetic
HIV+ diabetic
HIV- diabetic
UMAP 2
UMAP 1
D
CCDC80
COL1A2
CD68
CD1C
ACTA2
CLDN5
NKG7
CD3E
Stromal
Myeloid
Vascular
Lymphoid
UMAP 2
UMAP 1
E
% Total cells
p = 0.004
HIV+ non-diabetic
HIV+ prediabetic
HIV+ diabetic
HIV- diabetic
Stromal
Vascular
Myeloid
Lymphoid

Figure 1. Single-cell RNA sequencing reveals disease-specific heterogeneity of subcutaneous white adipose tissue. a, Schematic overview of study design. Twenty HIV+ non-diabetic, 19 HIV+ prediabetic, 20 HIV+ diabetic, and 32 HIV- diabetic participants underwent abdominal subcutaneous adipose tissue harvesting with liposuction. Tissue was processed with collagenase and dissociated. Single-cell suspensions from each participant were hashed and labeled with CITE-seq antibodies before multiplexing in groups of four. 10x libraries were generated using the Chromium platform and sequenced on Illumina NovaSeq 6000. The bioinformatic pipeline included demultiplexing, quality control, dimensional reduction and clustering, and differential gene testing. **b**, Uniform Manifold and Project (UMAP) of 283,491 cells from 91 individuals after removal of doublets and quality control, with manual annotation of cell clusters based on canonical gene markers. **c,** UMAP after harmony integration split by disease status showing successful integration; HIV+ non-diabetic (red), HIV+ prediabetic (orange), HIV+ diabetic (gold) and HIV- diabetic (blue). **d**, Gene expression projected on the UMAP identifying major cell types including stromal (*COL1A2, CCDC80*), vascular (*CLDN5, ACTA2*), myeloid (CD68, CD1C), T cell and natural killer cells (*CD3E, NKG7*). **e**, Boxplot showing the proportion of major cell categories (stromal, vascular, lymphoid, and myeloid) as a percentage of total cells split by disease status (HIV+ non-diabetic, red; HIV+ prediabetic, orange; HIV+ diabetic, gold; HIV- diabetic; blue). The horizontal black line represents the median, the box shows the lower and upper quartile limits and the whiskers are 1.5x the interquartile range.
Abbreviations: cMo, classical monocyte; cDC1, conventional dendritic cell type 1; cDC2B, conventional dendritic cell type 2B; DC, dendritic cell; EC, endothelial cell; ECM, extracellular matrix; EndoMT, endothelial-mesenchymal transitional; ILC, innate lymphoid cell; IFN+, interferon; LAM, lipid-associated macrophage; Mac, macrophage; mNK, mature natural killer; Mo, monocyte; NK, natural killer; nMo, non-classical monocyte; pDC, plasmacytoid dendritic cell; PVM, perivascular macrophage; TEMRA, T effector memory RA; VSMC, vascular smooth muscle

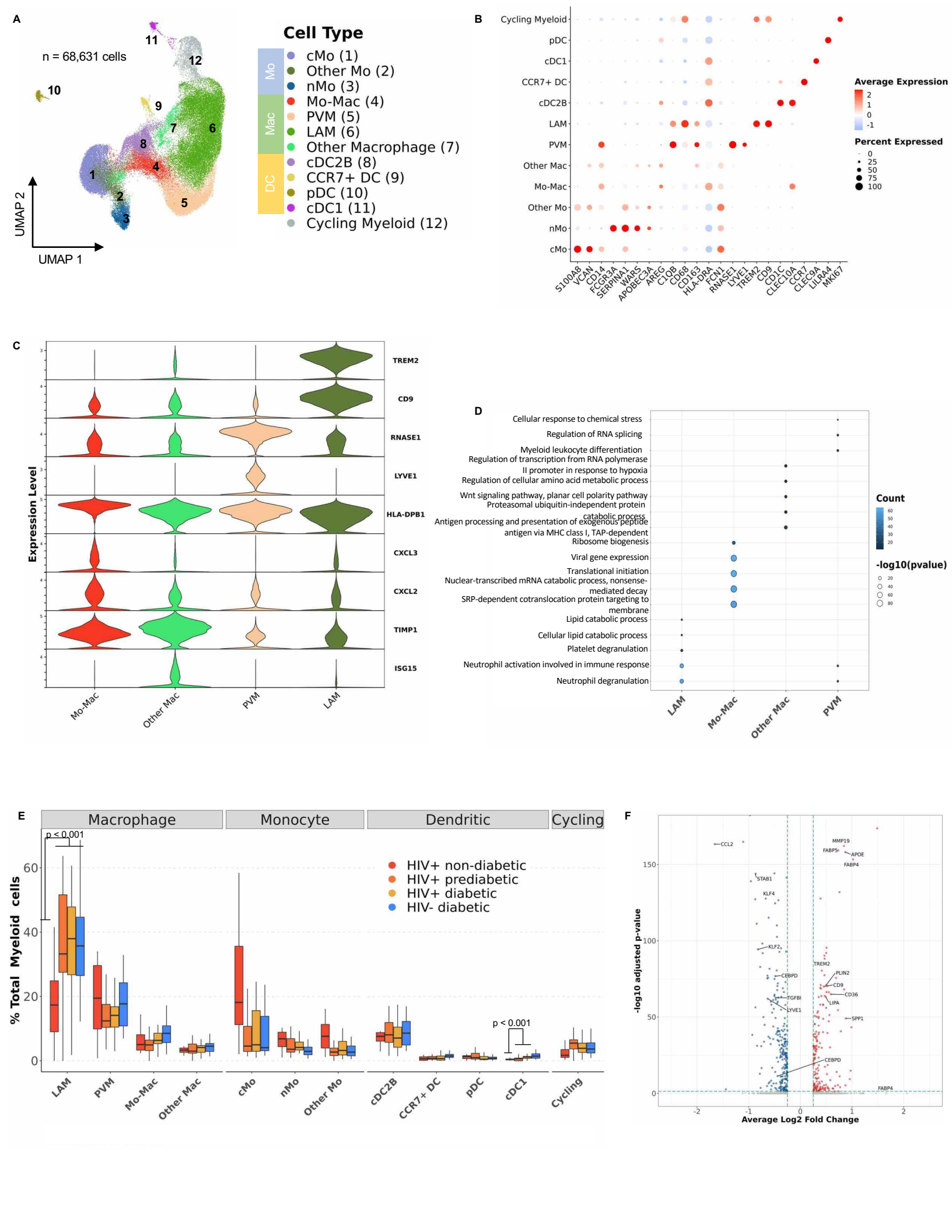
A
n = 68,631 cells
Cell Type
Mo
Mac
DC
cMo (1)
Other Mo (2)
nMo (3)
Mo-Mac (4)
PVM (5)
LAM (6)
Other Macrophage (7)
cDC2B (8)
CCR7+ DC (9)
pDC (10)
cDC1 (11)
Cycling Myeloid (12)
UMAP 1
UMAP 2
B
Cycling Myeloid
pDC
cDC1
CCR7+ DC
cDC2B
LAM
PVM
Other Mac
Mo-Mac
Other Mo
nMo
cMo
S100A8
VCAN
CD14
FCGR3A
SERPINA1
WARS
APOBEC3A
AREG
C1QB
CD68
CD163
HLA-DRA
FCN1
RNASE1
LYVE1
TREM2
CD9
CD1C
CLEC10A
CCR7
CLEC9A
LILRA4
MKI67
Average Expression
Percent Expressed
C
TREM2
CD9
RNASE1
LYVE1
HLA-DPB1
CXCL3
CXCL2
TIMP1
ISG15
Expression Level
Mo-Mac
Other Mac
PVM
LAM
D
Cellular response to chemical stress
Regulation of RNA splicing
Myeloid leukocyte differentiation
Regulation of transcription from RNA polymerase II promoter in response to hypoxia
Regulation of cellular amino acid metabolic process
Wnt signaling pathway, planar cell polarity pathway
Proteasomal ubiquitin-independent protein catabolic process
Antigen processing and presentation of exogenous peptide antigen via MHC class I, TAP-dependent
Ribosome biogenesis
Viral gene expression
Translational initiation
Nuclear-transcribed mRNA catabolic process, nonsense-mediated decay
SRP-dependent cotranslocation protein targeting to membrane
Lipid catabolic process
Cellular lipid catabolic process
Platelet degranulation
Neutrophil activation involved in immune response
Neutrophil degranulation
LAM
Mo-Mac
Other Mac
PVM
Count
-log10(pvalue)
E
Macrophage
Monocyte
Dendritic
Cycling
p < 0.001
HIV+ non-diabetic
HIV+ prediabetic
HIV+ diabetic
HIV- diabetic
% Total Myeloid cells
LAM
PVM
Mo-Mac
Other Mac
cMo
nMo
Other Mo
cDC2B
CCR7+ DC
pDC
cDC1
Cycling
F
CCL2
MMP19
FABP5
APOE
FABP4
STAB1
KLF4
KLF2
TREM2
CEBPD
PLIN2
CD9
CD36
TGFBI
LIPA
LYVE1
SPP1
CEBPD
FABP4
-log10 adjusted p-value
Average Log2 Fold Change

Figure 2. Lipid-associated macrophages accumulate with glucose intolerance regardless of HIV serostatus. a, Uniform Manifold Approximation and Projection (UMAP) of myeloid cells (n = 68,631) from 91 individuals after subsetting and reclustering showing 12 distinct cell types/states. **b**, Dot plot showing selected gene markers on the x-axis and cell type on the y-axis. The dot size reflects the percentage of cells expressing the gene while the color reflects the scaled average expression. **c**, Violin Plot with macrophage subtype on the x-axis and scaled expression of *TREM2, CD9, RNASE1, LYVE1, HLA-DBP1, CXCL3, CXCL2, TIMP1,* and *ISG15.* **d,** Gene Ontology (GO) over-representation analysis with macrophage subtype on the x-axis and GO on the y-axis. The size of the circle denotes the negative $\log_{10}$ p-value while the color denotes the number of genes assigned to the pathway. **e,** Boxplot showing the proportion of each cell type as a percent of total myeloid cells split by disease state (HIV+ non-diabetic, red; HIV+ prediabetic, orange; HIV+ diabetic, gold; HIV- diabetic; blue). Cell types are broadly categorized as macrophage, monocyte, dendritic, or cycling and are ordered by proportion. The horizontal line represents the median proportion and the box depicts the lower and upper quartile limits. The whiskers are 1.5x the interquartile range. **f,** Differentially expressed genes in macrophages comparing diabetic persons with HIV (reference) with non-diabetic persons with HIV plotted as $\log_2$ fold change (x-axis) vs negative $\log_{10}$ FDR-adjusted p-value (y-axis). Genes with higher expression in diabetic persons with HIV are colored red while genes with lower expression are colored blue. Abbreviations: cMo, classical monocytes; cDC1, conventional dendritic cell type 1; cDC2B, conventional dendritic cell type 2B; DC, dendritic cell; LAM, lipid-associated macrophage; Mac, macrophage; Mo, monocyte; PVM, perivascular macrophage; pDC, plasmacytoid dendritic cell

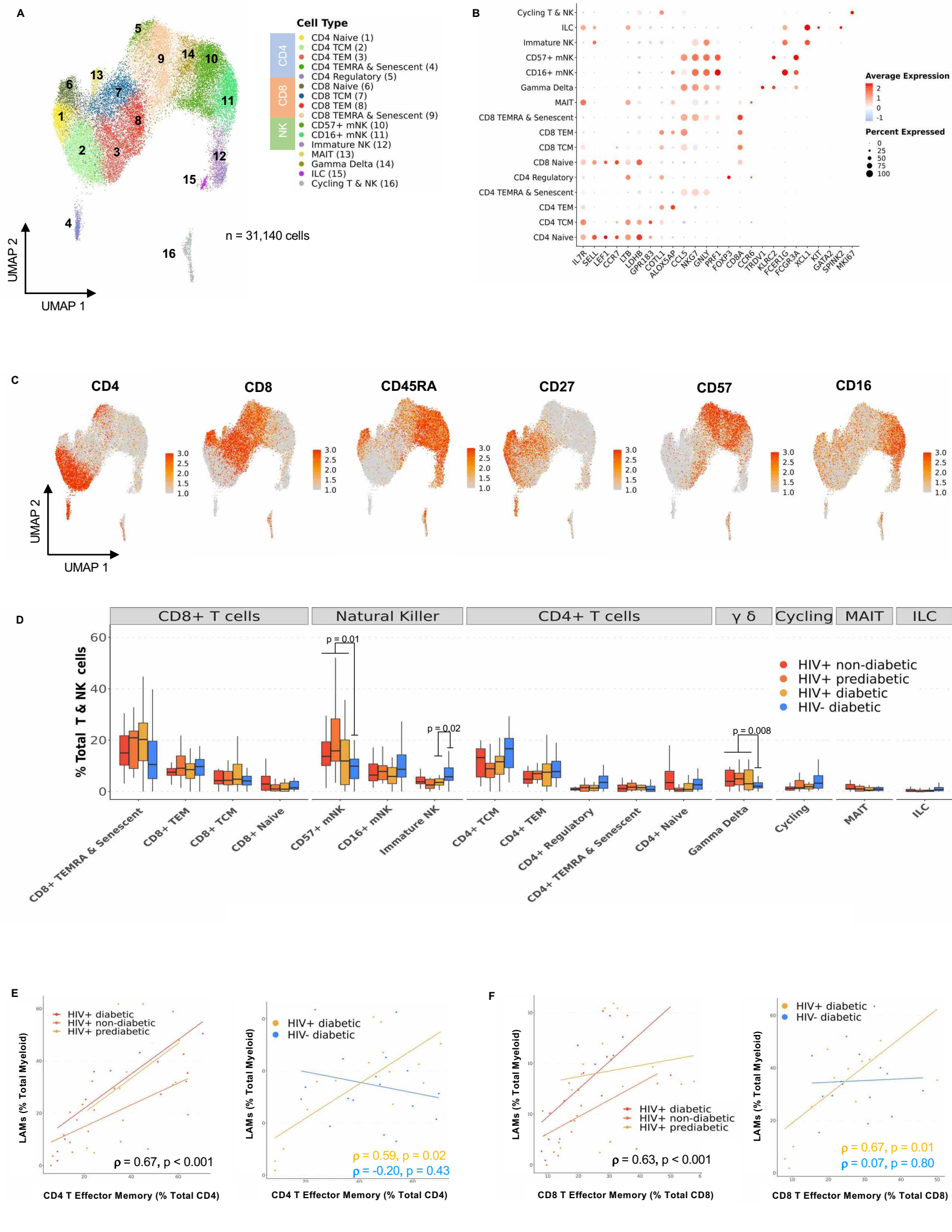
A
Cell Type
CD4
CD8
NK
CD4 Naive (1)
CD4 TCM (2)
CD4 TEM (3)
CD4 TEMRA & Senescent (4)
CD4 Regulatory (5)
CD8 Naive (6)
CD8 TCM (7)
CD8 TEM (8)
CD8 TEMRA & Senescent (9)
CD57+ mNK (10)
CD16+ mNK (11)
Immature NK (12)
MAIT (13)
Gamma Delta (14)
ILC (15)
Cycling T & NK (16)
n = 31,140 cells
UMAP 2
UMAP 1
B
Average Expression
Percent Expressed
Cycling T & NK
ILC
Immature NK
CD57+ mNK
CD16+ mNK
Gamma Delta
MAIT
CD8 TEMRA & Senescent
CD8 TEM
CD8 TCM
CD8 Naive
CD4 Regulatory
CD4 TEMRA & Senescent
CD4 TEM
CD4 TCM
CD4 Naive
IL7R SELL LEF1 CCR7 LTB LDHB GPR183 COTL1 ALOX5AP CCL5 NKG7 GNLY PRF1 FOXP3 CD8A CCR6 TRDV1 KLRC2 FCER1G FCGR3A XCL1 KIT GATA2 SPINK2 MKI67
C
CD4
CD8
CD45RA
CD27
CD57
CD16
UMAP 2
UMAP 1
D
CD8+ T cells
Natural Killer
CD4+ T cells
γ δ
Cycling
MAIT
ILC
% Total T & NK cells
HIV+ non-diabetic
HIV+ prediabetic
HIV+ diabetic
HIV- diabetic
p = 0.01
p = 0.02
p = 0.008
CD8+ TEMRA & Senescent
CD8+ TEM
CD8+ TCM
CD8+ Naive
CD57+ mNK
CD16+ mNK
Immature NK
CD4+ TCM
CD4+ TEM
CD4+ Regulatory
CD4+ TEMRA & Senescent
CD4+ Naive
Gamma Delta
Cycling
MAIT
ILC
E
HIV+ diabetic
HIV+ non-diabetic
HIV+ prediabetic
LAMs (% Total Myeloid)
ρ = 0.67, p < 0.001
CD4 T Effector Memory (% Total CD4)
HIV+ diabetic
HIV- diabetic
ρ = 0.59, p = 0.02
ρ = -0.20, p = 0.43
CD4 T Effector Memory (% Total CD4)
F
HIV+ diabetic
HIV+ non-diabetic
HIV+ prediabetic
ρ = 0.63, p < 0.001
CD8 T Effector Memory (% Total CD8)
HIV+ diabetic
HIV- diabetic
ρ = 0.67, p = 0.01
ρ = 0.07, p = 0.80
CD8 T Effector Memory (% Total CD8)

Figure 3. CD4 and CD8 T Effector Memory Proportion Increases with Glucose Intolerance in Persons with HIV. a, Uniform Manifold Approximation and Projection (UMAP) of T cells, natural killer cells, and innate lymphoid cells (n = 31,140 cells) from 91 individuals after subsetting and reclustering showing 16 distinct cell types/states. **b**, Dot plot showing selected gene markers on the x-axis and cell type on the y-axis. The dot size reflects the percentage of cells expressing the gene while the color reflects the scaled average expression. **c**, UMAP with CITE-seq surface antibodies for CD4, CD8, CD57, CD45RA, CD27, and CD16. **d,** Boxplot showing the proportion of each cell type as a percent of total lymphoid cells split by disease state (HIV+ non-diabetic, red; HIV+ prediabetic, orange; HIV+ diabetic, gold; HIV- diabetic; blue). Cell types are broadly categorized as T cells, natural killer cells, cycling, MAIT, gamma delta, and innate lymphoid cells and are ordered by proportion. The horizontal line represents the median proportion and the box depicts the lower and upper quartile limits. The whiskers are 1.5x the interquartile range. **e** Spearman's correlation between $CD4^+$ T_{EM} cells and lipid associated macrophages with $CD4^+$ T_{EM} cells plotted on the x-axis (as a percentage of total $CD4^+$ T cells) and lipid associated macrophages plotted on the y-axis (as a percentage of total myeloid) for both HIV+ (left) and diabetic (right) persons. **f,** Spearman's correlation between $CD8^+$ T_{EM} cells and lipid associated macrophages with $CD8^+$ T_{EM} cells plotted on the x-axis (as a percentage of total $CD8^+$ T cells) and lipid associated macrophages plotted on the y-axis (as a percentage of total myeloid) for both HIV+ (left) and diabetic (right) persons. Abbreviations: ILC, innate lymphoid cells; mNK, mature natural killer; NK, natural killer; TCM, T central memory; TEM, T effector memory; TEMRA, T effector memory RA+

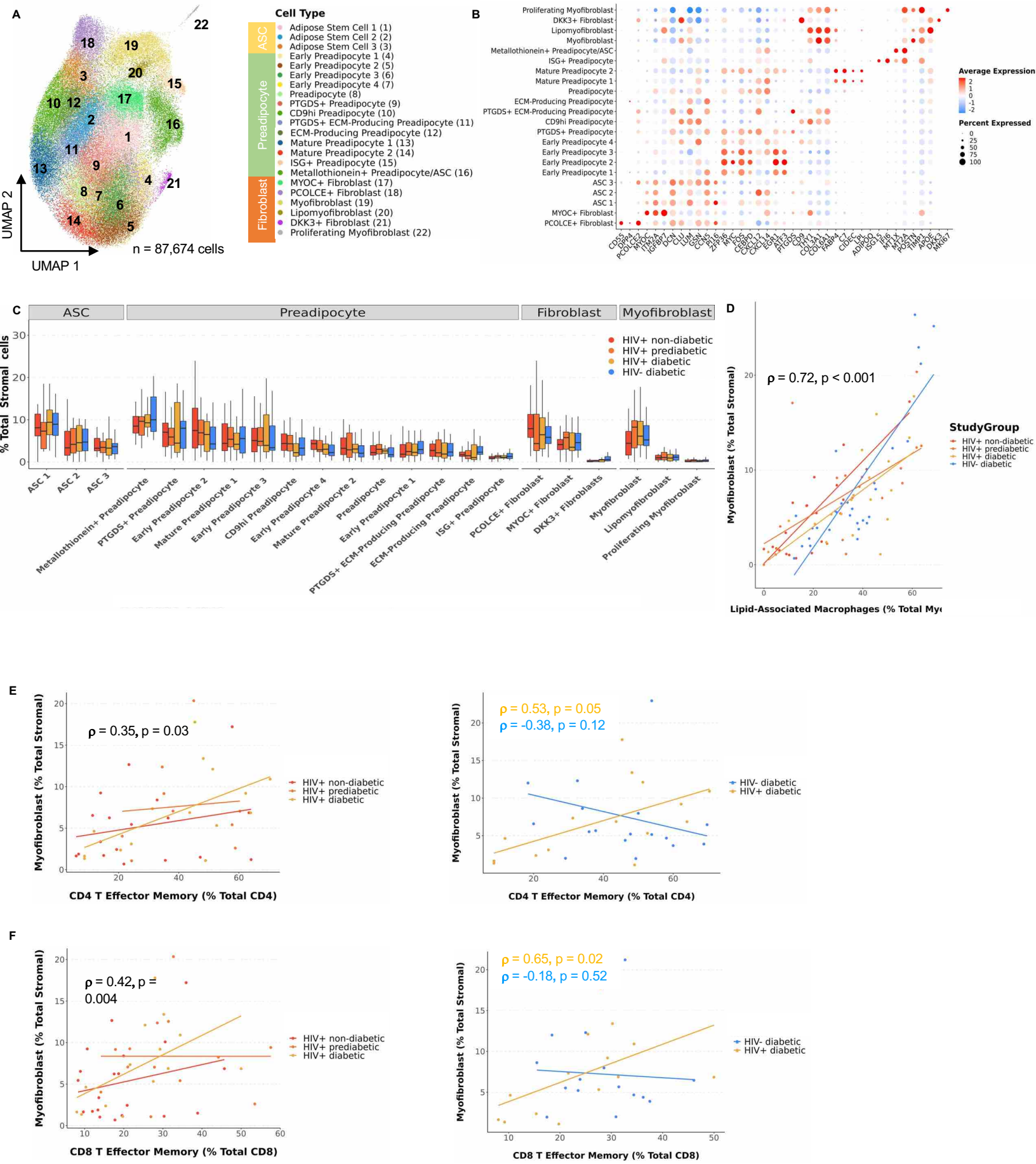
A
UMAP 1
UMAP 2
n = 87,674 cells
Cell Type
ASC
Preadipocyte
Fibroblast
Adipose Stem Cell 1 (1)
Adipose Stem Cell 2 (2)
Adipose Stem Cell 3 (3)
Early Preadipocyte 1 (4)
Early Preadipocyte 2 (5)
Early Preadipocyte 3 (6)
Early Preadipocyte 4 (7)
Preadipocyte (8)
PTGDS+ Preadipocyte (9)
CD9hi Preadipocyte (10)
PTGDS+ ECM-Producing Preadipocyte (11)
ECM-Producing Preadipocyte (12)
Mature Preadipocyte 1 (13)
Mature Preadipocyte 2 (14)
ISG+ Preadipocyte (15)
Metallothionein+ Preadipocyte/ASC (16)
MYOC+ Fibroblast (17)
PCOLCE+ Fibroblast (18)
Myofibroblast (19)
Lipomyofibroblast (20)
DKK3+ Fibroblast (21)
Proliferating Myofibroblast (22)
B
Average Expression
Percent Expressed
C
ASC
Preadipocyte
Fibroblast
Myofibroblast
% Total Stromal cells
HIV+ non-diabetic
HIV+ prediabetic
HIV+ diabetic
HIV- diabetic
D
ρ = 0.72, p < 0.001
Myofibroblast (% Total Stromal)
Lipid-Associated Macrophages (% Total My
StudyGroup
HIV+ non-diabetic
HIV+ prediabetic
HIV+ diabetic
HIV- diabetic
E
ρ = 0.35, p = 0.03
CD4 T Effector Memory (% Total CD4)
ρ = 0.53, p = 0.05
ρ = -0.38, p = 0.12
F
ρ = 0.42, p = 0.004
CD8 T Effector Memory (% Total CD8)
ρ = 0.65, p = 0.02
ρ = -0.18, p = 0.52

Figure 4. Lipid Associated Macrophages are Associated with Higher Proportion of Myofibroblasts. a, Uniform Manifold Approximation and Projection (UMAP) of stromal cells (n = 87,674) from 91 individuals after subsetting and reclustering. **b**, Dot plot of stromal cells showing selected gene markers on the x axis and cell type on the y axis. The dot size reflects the percentage of cells expressing the gene while the color reflects the scaled average expression. **c**, Boxplot showing the proportion of each cell type as a percent of total stromal cells split by disease state (HIV+ non-diabetic, red; HIV+ prediabetic, orange; HIV+ diabetic, gold; HIV- diabetic; blue). The horizontal line represents the median proportion and the box depicts the lower and upper quartile limits. The whiskers are 1.5x the interquartile range. **d,** Scatter plot with lipid-associated macrophages (as a percent of total myeloid) on the x axis and myofibroblast (as a percent of total stromal) on the y-axis. The Spearman's correlation for all participants is significant ($p = 0.72$, $p < 0.001$). A regression line was added to the scatter plot split by disease state (HIV+ non-diabetic, red; HIV+ prediabetic, orange; HIV+ diabetic, gold; HIV- diabetic; blue). **e,** Scatter plot with $CD4^+$ effector memory cells (as a percent of total $CD4^+$ T cells) on the x axis and myofibroblast (as a percent of total stromal) for HIV+ (left) split by disease state (HIV+ non-diabetic, red; HIV+ prediabetic, orange; HIV+ diabetic, gold) and diabetics (right) split by HIV serostatus (HIV+ diabetic, gold; HIV- diabetic, blue). **f,** Scatter plot with $CD8^+$ effector memory cells (as a percent of total $CD8^+$ T cells) on the x axis and myofibroblast (as a percent of total stromal) for HIV+ (left) split by disease state (HIV+ non-diabetic, red; HIV+ prediabetic, orange; HIV+ diabetic, gold) and diabetics (right) split by HIV serostatus (HIV+ diabetic, gold; HIV- diabetic, blue). Abbreviations: ASC, Adipose Stem Cell; ECM, extracellular matrix

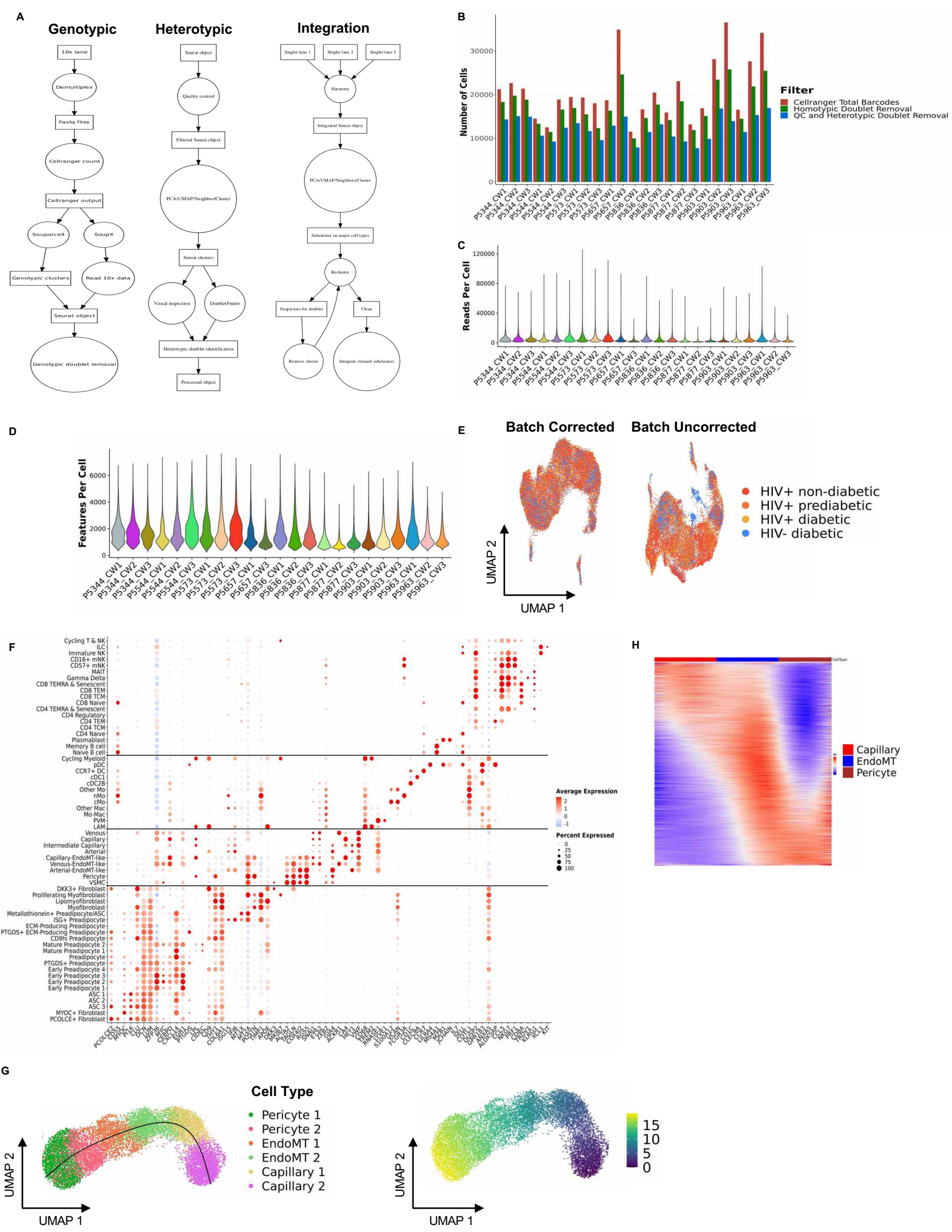
A
Genotypic
Heterotypic
Integration
10x lane
Demultiplex
Fastq files
Cellranger count
Cellranger output
Souporcell
SoupX
Genotypic clusters
Read 10x data
Seurat object
Genotypic doublet removal
Seurat object
Quality control
Filtered Seurat object
PCA/UMAP/Neighbor/Cluster
Seurat clusters
Visual inspection
DoubletFinder
Heterotypic doublet identification
Processed object
Singlet lane 1
Singlet lane 2
Singlet lane 3
Harmony
Integrated Seurat object
PCA/UMAP/Neighbor/Cluster
Subcluster on major cell types
Recluster
Suspicious for doublet
Clean
Remove cluster
Integrate cleaned subclusters
B
Number of Cells
Filter
Cellranger Total Barcodes
Homotypic Doublet Removal
QC and Heterotypic Doublet Removal
C
Reads Per Cell
D
Features Per Cell
E
Batch Corrected
Batch Uncorrected
HIV+ non-diabetic
HIV+ prediabetic
HIV+ diabetic
HIV- diabetic
UMAP 2
UMAP 1
F
Average Expression
Percent Expressed
H
Capillary
EndoMT
Pericyte
G
Cell Type
Pericyte 1
Pericyte 2
EndoMT 1
EndoMT 2
Capillary 1
Capillary 2
UMAP 2
UMAP 1

Supplemental Figure 1. Bioinformatic Pipeline and Quality Metrics. a, Flow diagram of bioinformatic pipeline split into three sections: Homotypic doublet identification, heterotypic doublet identification, and integration and downstream processing. The Illumina NovaSeq 6000 Bcl files were demultiplexed into raw fastq files. Fastq files were aligned to the Human Genome Reference Consortium Build 38 (hg38) and cells were called using the Cell Ranger count function with default settings. Soupx was used to remove ambient RNA and the corrected count matrices were used to create a Seurat object. Simultaneously, Souporcell was used to genetically demultiplex the samples. Doublets identified by Souporcell were removed. Next, each Seurat object underwent quality control filtering and downstream dimensional reduction and clustering. Clusters were visually inspected and labeled as transcriptional doublets based on co-expression of major cell types and/or consisting of many doublets identified by DoubletFinder. The processed objects were then integrated using Harmony correction on the principal components prior to clustering. Cells were subclustered based on major cell lineages and transcriptional doublets were iteratively removed prior to reintegration. **b,** Barplot graph showing each lane (x-axis) and number of cells (y-axis). The graph is split by the total barcodes identified by Cell Ranger (red), the cells remaining after genetic demultiplexing and removal of homotypic doublets (green), and the cells remaining after applying quality control filters and removing transcriptional doublets (blue). **c,** Distribution of read counts per cell (y-axis) by lane (x-axis). **d,** Distribution of the number of features (genes) per cell (y-axis) by lane (x-axis). **e,** Example of batch effect subclustering on T cells shown in a Uniform Manifold Approximation and Projection split by metabolic and HIV status: HIV+ non-diabetic (red), HIV+ prediabetic (orange), HIV+ diabetic (gold), HIV- diabetic (blue). After harmony correction, cells from each group are more uniformly distributed. **f,** Dot plot with selected genes on the x axis and cell type on the y axis. The size of the dot represents the percentage of cells with expression of that gene and the color of the dot represents the average expression level for that gene. **g,** Slingshot trajectory with capillary 2 as the root embedded on the UMAP (top) and Slingshot pseudotime (bottom). **h,** Scaled gene expressed ordered by pseudotime.

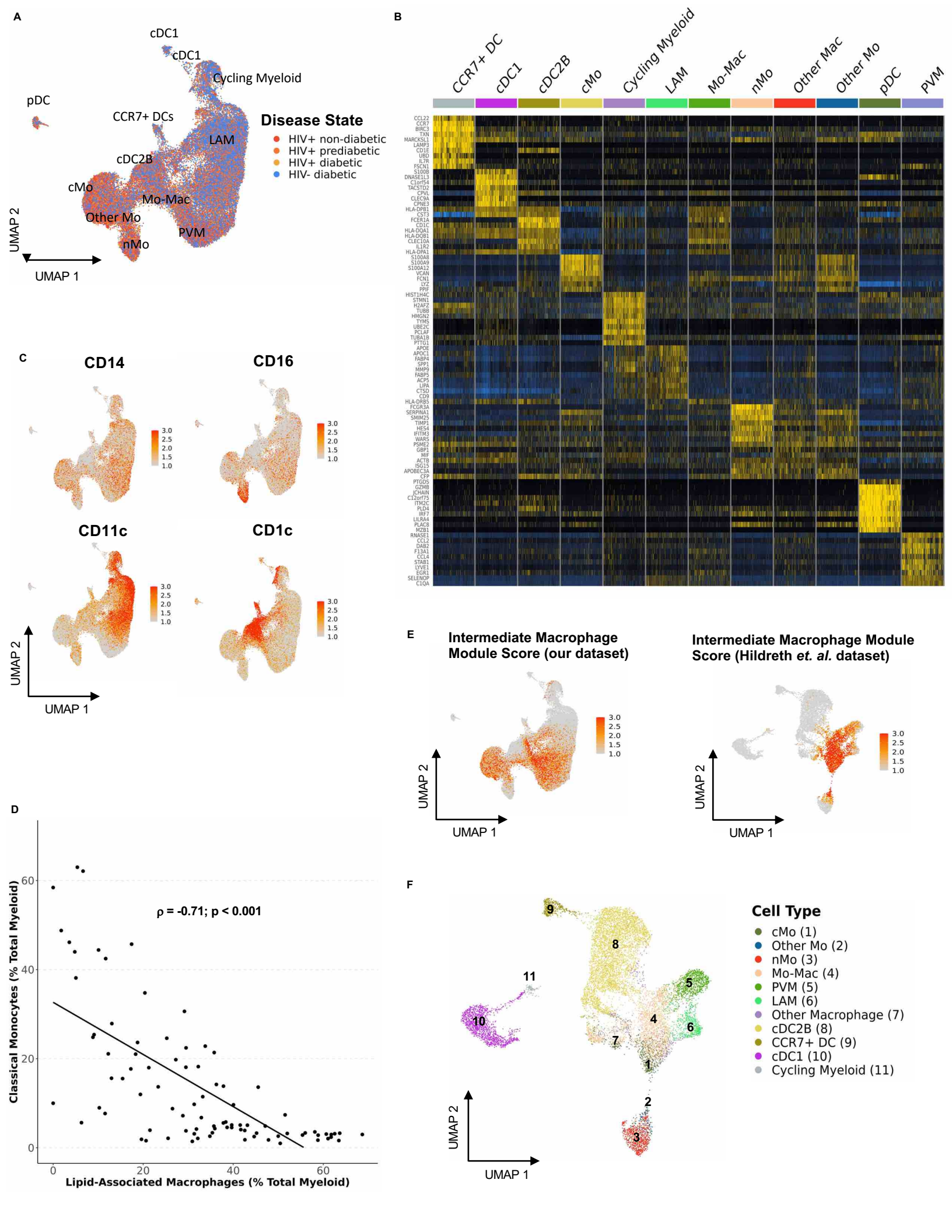
A
cDC1
cDC1
Cycling Myeloid
pDC
CCR7+ DCs
LAM
cDC2B
cMo
Mo-Mac
Other Mo
PVM
nMo
UMAP 2
UMAP 1
Disease State
HIV+ non-diabetic
HIV+ prediabetic
HIV+ diabetic
HIV- diabetic
B
CCR7+ DC
cDC1
cDC2B
cMo
Cycling Myeloid
LAM
Mo-Mac
nMo
Other Mac
Other Mo
pDC
PVM
C
CD14
CD16
CD11c
CD1c
3.0
2.5
2.0
1.5
1.0
UMAP 2
UMAP 1
D
ρ = -0.71; p < 0.001
Classical Monocytes (% Total Myeloid)
Lipid-Associated Macrophages (% Total Myeloid)
0
20
40
60
E
Intermediate Macrophage Module Score (our dataset)
Intermediate Macrophage Module Score (Hildreth et. al. dataset)
UMAP 2
UMAP 1
F
Cell Type
cMo (1)
Other Mo (2)
nMo (3)
Mo-Mac (4)
PVM (5)
LAM (6)
Other Macrophage (7)
cDC2B (8)
CCR7+ DC (9)
cDC1 (10)
Cycling Myeloid (11)
1
2
3
4
5
6
7
8
9
10
11
UMAP 2
UMAP 1

Supplemental Figure 2. Myeloid Cluster. a, Uniform Manifold Projection and Approximation (UMAP) of myeloid cells after downstream analysis on harmony-corrected principal components grouped by metabolic and HIV status: HIV+ non-diabetic (red), HIV+ prediabetic (orange), HIV+ diabetic (gold), HIV- diabetic (blue). **b,** Heatmap of scaled gene expression of the top 10 genes defining each annotated cluster using model-based analysis of single cell transcriptomics (MAST). **c,** UMAP with CITE-seq surface antibodies for CD14 (classical monocytes), CD16 (non-classical monocytes), CD1C (dendritic cells), CD11C (lipid associated macrophages). **d,** Scatter plot with lipid-associated macrophage as a percentage of total myeloid on the x-axis and classical monocytes as a percent of total myeloid on the y-axis showing significant inverse correlation by Spearman's test ($\rho = -0.71$, $p < 0.001$**) . e,** UMAP of myeloid cells with superimposed intermediate macrophage score on the current dataset (left) and Hildreth *et. al.* dataset (right). The score was derived using the AddModuleScore function implemented in Seurat by taking genes expressed > 2 fold in the intermediate macrophage population from Hildreth *et. al*. **f,** Seurat reference-based label transfer from the current study to Hildreth *et. al.* [S1]. Abbreviations: cMo, classical monocyte; cDC1, conventional dendritic cell type 1; cDC2B, conventional dendritic cell type 2B; DC, dendritic cell; IM, intermediate macrophage; LAM, lipid-associated macrophage; Mac, macrophage; Mo, monocyte; nMo, non-classical macrophage; PVM, perivascular macrophage; pDC, plasmacytoid dendritic cell

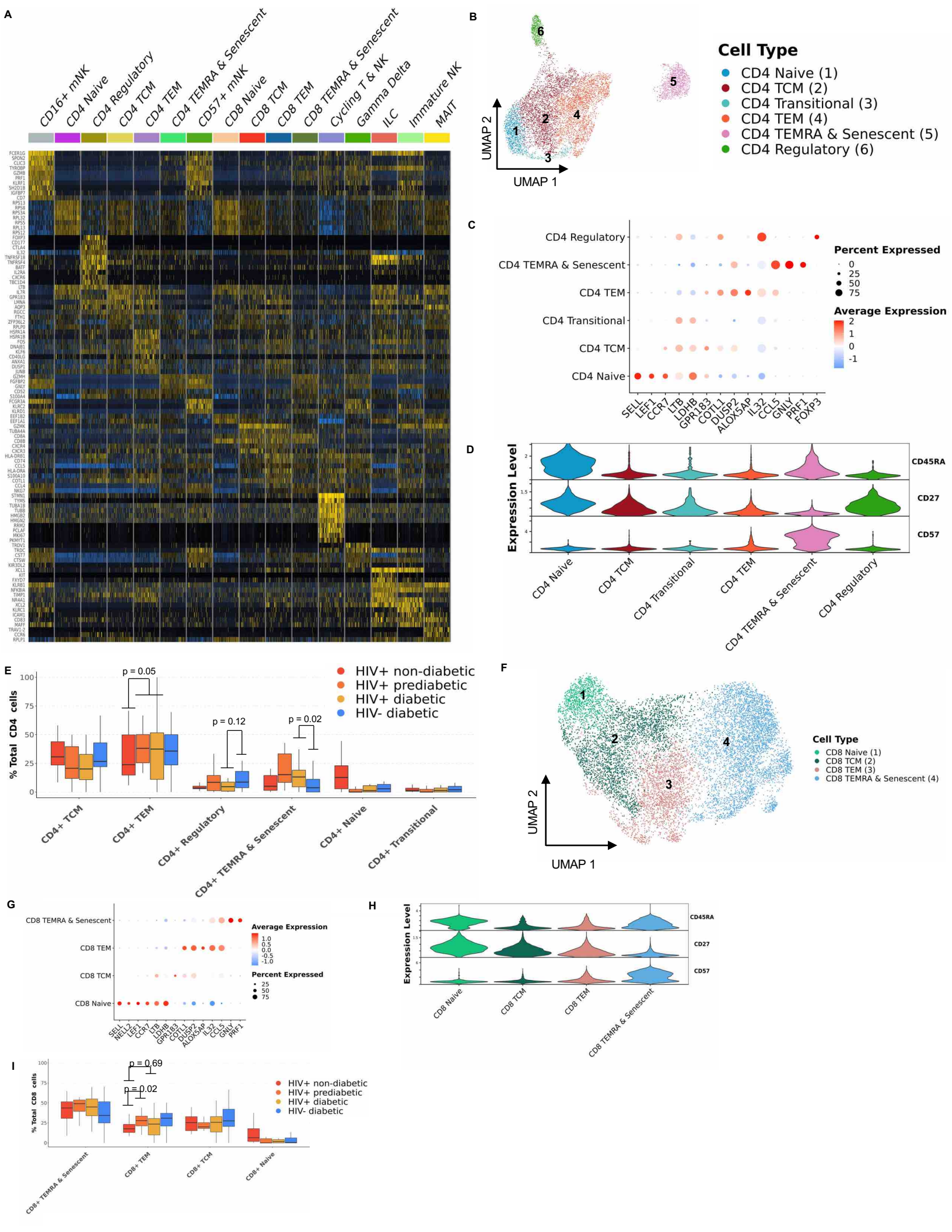
A
CD16+ mNK
CD4 Naive
CD4 Regulatory
CD4 TCM
CD4 TEM
CD4 TEMRA & Senescent
CD57+ mNK
CD8 Naive
CD8 TCM
CD8 TEM
CD8 TEMRA & Senescent
Cycling T & NK
Gamma Delta
ILC
Immature NK
MAIT
B
Cell Type
CD4 Naive (1)
CD4 TCM (2)
CD4 Transitional (3)
CD4 TEM (4)
CD4 TEMRA & Senescent (5)
CD4 Regulatory (6)
UMAP 2
UMAP 1
C
CD4 Regulatory
CD4 TEMRA & Senescent
CD4 TEM
CD4 Transitional
CD4 TCM
CD4 Naive
SELL
LEF1
CCR7
LTB
LDHB
GPR183
COTL1
DUSP2
ALOX5AP
IL32
CCL5
GNLY
PRF1
FOXP3
Percent Expressed
Average Expression
D
Expression Level
CD45RA
CD27
CD57
CD4 Naive
CD4 TCM
CD4 Transitional
CD4 TEM
CD4 TEMRA & Senescent
CD4 Regulatory
E
% Total CD4 cells
p = 0.05
p = 0.12
p = 0.02
HIV+ non-diabetic
HIV+ prediabetic
HIV+ diabetic
HIV- diabetic
CD4+ TCM
CD4+ TEM
CD4+ Regulatory
CD4+ TEMRA & Senescent
CD4+ Naive
CD4+ Transitional
F
Cell Type
CD8 Naive (1)
CD8 TCM (2)
CD8 TEM (3)
CD8 TEMRA & Senescent (4)
UMAP 2
UMAP 1
G
CD8 TEMRA & Senescent
CD8 TEM
CD8 TCM
CD8 Naive
Average Expression
Percent Expressed
SELL
NELL2
LEF1
CCR7
LTB
LDHB
GPR183
COTL1
DUSP2
ALOX5AP
IL32
CCL5
GNLY
PRF1
H
Expression Level
CD45RA
CD27
CD57
CD8 Naive
CD8 TCM
CD8 TEM
CD8 TEMRA & Senescent
I
% Total CD8 cells
p = 0.69
p = 0.02
HIV+ non-diabetic
HIV+ prediabetic
HIV+ diabetic
HIV- diabetic
CD8+ TEMRA & Senescent
CD8+ TEM
CD8+ TCM
CD8+ Naive

Supplemental Figure 3. T and NK Cells. a, Heatmap of scaled gene expression of the top 10 genes defining each annotated cluster using model-based analysis of single cell transcriptomics (MAST). **b,** Uniform Manifold Approximation and Projection (UMAP) of $CD4^+$ T cells (n = 8,045 cells) subset from all T cells. **c**, Dot plot of $CD4^+$ T cells with selected genes on the x axis and cell type on the y axis. The size of the dot represents the percentage of cells with expression of that gene and the color of the dot represents the average expression level for that gene. **d,** Violin plots for CITE-seq expression of CD45RA, CD27, and CD57 with annotated cluster on the x-axis and expression level on the y-axis for $CD4^+$ T cells . **f,** Boxplot showing the proportion of each $CD4^+$ T cell type as a percent of total $CD4^+$ T cells split by disease state (HIV+ non-diabetic, red; HIV+ prediabetic, orange; HIV+ diabetic, gold; HIV- diabetic; blue). The horizontal line represents the median proportion and the box depicts the lower and upper quartile limits. The whiskers are 1.5x the interquartile range. **f,** UMAP of $CD8^+$ T cells (n = 11,325 cells) subset from all T cells. **g**, Dot plot of $CD8^+$ T cells with selected genes on the x axis and cell type on the y axis. The size of the dot represents the percentage of cells with expression of that gene and the color of the dot represents the average expression level for that gene. **h**, Violin plots for CITE-seq expression of CD45RA, CD27, and CD57 with annotated cluster on the x-axis and expression level on the y-axis for $CD8^+$ T cells. **i,** Boxplot showing the proportion of each $CD8^+$ T cell type as a percent of total $CD8^+$ T cells split by disease state (HIV+ non-diabetic, red; HIV+ prediabetic, orange; HIV+ diabetic, gold; HIV- diabetic; blue). The horizontal line represents the median proportion and the box depicts the lower and upper quartile limits. The whiskers are 1.5x the interquartile range. Abbreviations: ILC, innate lymphoid cells; mNK, mature natural killer; NK, natural killer; TCM, T central memory; TEM, T effector memory, TEMRA, T effector memory RA^+

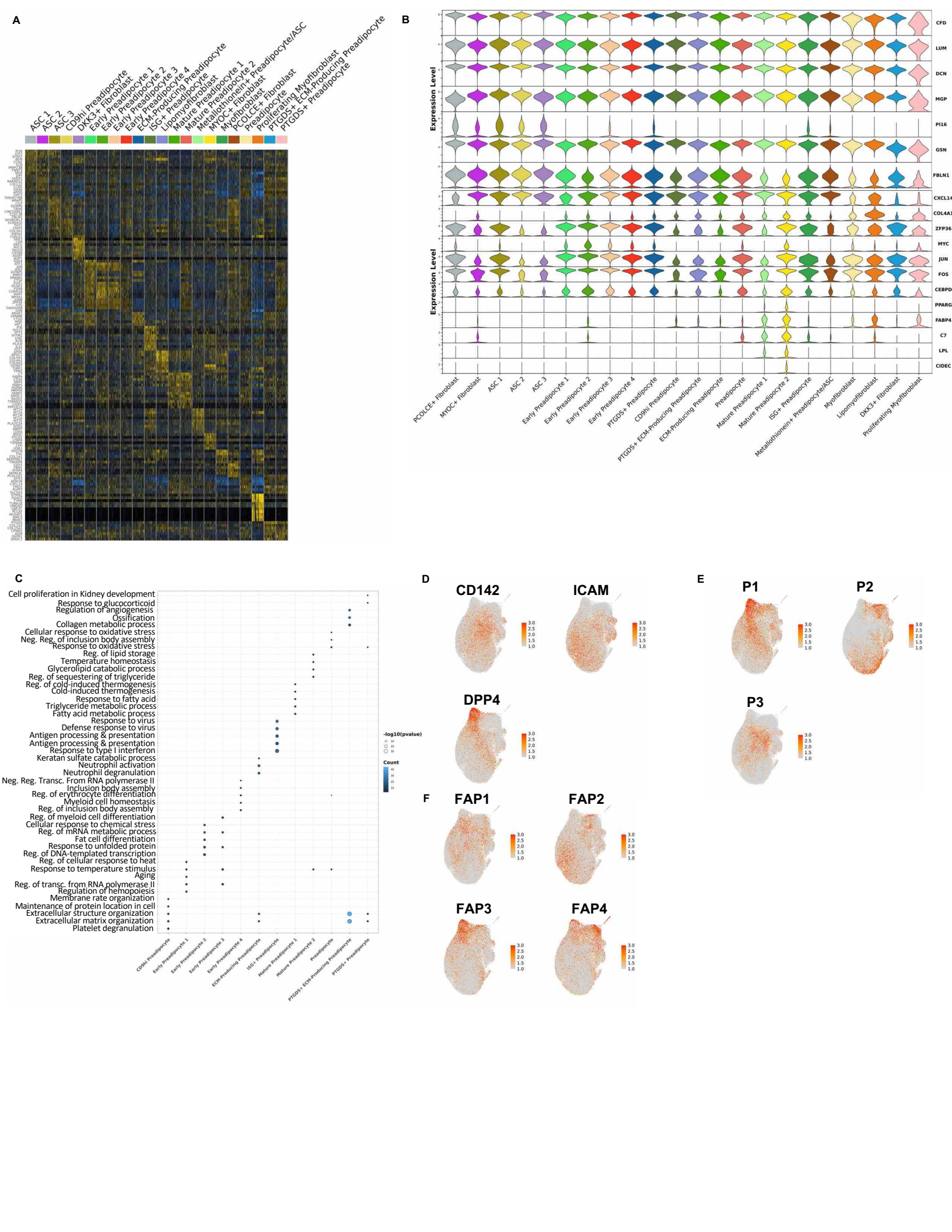
A
ASC 1
ASC 2
ASC 3
CD9hi Preadipocyte
DKK3+ Fibroblast
Early Preadipocyte 1
Early Preadipocyte 2
Early Preadipocyte 3
Early Preadipocyte 4
ECM-Producing Preadipocyte
Lipomyofibroblast
Mature Preadipocyte 1
Mature Preadipocyte 2
Metallothionein+ Preadipocyte/ASC
MYOC+ Fibroblast
Myofibroblast
PCOLCE+ Fibroblast
Preadipocyte
Proliferating Myofibroblast
PTGDS+ ECM-Producing Preadipocyte
PTGDS+ Preadipocyte
B
Expression Level
CFD
LUM
DCN
MGP
PI16
GSN
FBLN1
CXCL14
COL4A1
ZFP36
MYC
JUN
FOS
CEBPD
PPARG
FABP4
C7
LPL
CIDEC
PCOLCE+ Fibroblast
MYOC+ Fibroblast
ASC 1
ASC 2
ASC 3
Early Preadipocyte 1
Early Preadipocyte 2
Early Preadipocyte 3
Early Preadipocyte 4
PTGDS+ Preadipocyte
CD9hi Preadipocyte
PTGDS+ ECM-Producing Preadipocyte
ECM-Producing Preadipocyte
Preadipocyte
Mature Preadipocyte 1
Mature Preadipocyte 2
ISG+ Preadipocyte
Metallothionein+ Preadipocyte/ASC
Myofibroblast
Lipomyofibroblast
DKK3+ Fibroblast
Proliferating Myofibroblast
C
Cell proliferation in Kidney development
Response to glucocorticoid
Regulation of angiogenesis
Ossification
Collagen metabolic process
Cellular response to oxidative stress
Neg. Reg. of inclusion body assembly
Response to oxidative stress
Reg. of lipid storage
Temperature homeostasis
Glycerolipid catabolic process
Reg. of sequestering of triglyceride
Reg. of cold-induced thermogenesis
Cold-induced thermogenesis
Response to fatty acid
Triglyceride metabolic process
Fatty acid metabolic process
Response to virus
Defense response to virus
Antigen processing & presentation
Antigen processing & presentation
Response to type I interferon
Keratan sulfate catabolic process
Neutrophil activation
Neutrophil degranulation
Neg. Reg. Transc. From RNA polymerase II
Inclusion body assembly
Reg. of erythrocyte differentiation
Myeloid cell homeostasis
Reg. of inclusion body assembly
Reg. of myeloid cell differentiation
Cellular response to chemical stress
Reg. of mRNA metabolic process
Fat cell differentiation
Response to unfolded protein
Reg. of DNA-templated transcription
Reg. of cellular response to heat
Response to temperature stimulus
Aging
Reg. of transc. from RNA polymerase II
Regulation of hemopoiesis
Membrane rate organization
Maintenance of protein location in cell
Extracellular structure organization
Extracellular matrix organization
Platelet degranulation
-log10(pvalue)
Count
CD9hi Preadipocyte
Early Preadipocyte 1
Early Preadipocyte 2
Early Preadipocyte 3
Early Preadipocyte 4
ECM-Producing Preadipocyte
ISG+ Preadipocyte
Mature Preadipocyte 1
Mature Preadipocyte 2
Preadipocyte
PTGDS+ ECM-Producing Preadipocyte
PTGDS+ Preadipocyte
D
CD142
ICAM
DPP4
E
P1
P2
P3
F
FAP1
FAP2
FAP3
FAP4

Supplemental Figure 4. Fibro-Adipogenic Cells. a, Heatmap of scaled gene expression of the top 10 genes defining each annotated stromal cluster using model-based analysis of single cell transcriptomics (MAST). **b,** Violin plot of scaled expression of *CFD, DCN, LUM, MGP, PI16, GSN, and FBLN1* that are markers of progenitor cells (y axis) by cluster (x axis) and scaled expression of *CXCL14, COL4A1, ZFP36, MYC, JUN, FOS, CEBPD, PPARG, FABP4, C7, LPL, and CIDEC* that are markers of preadipocytes (y axis) by cluster (x axis). **c,** Gene Ontology (GO) over-representation analysis with preadipocyte cluster on the x-axis and GO pathway and the y-axis. The size of the circle denotes the negative $\log_{10}$ p-value while the color denotes the number of genes assigned to the pathway. **d,** Scaled module score using gene markers that identify CD142+ (top left), ICAM+ (top right), and DPP4 (bottom left) clusters from Merrick *et. al.* superimposed on the fibro-adipogenic UMAP [S2]. **e,** Scaled module score using gene markers that identify P1 (top left), P2 (top right), and P3 (bottom left) clusters from Schwalie *et. al.* superimposed on the fibro-adipogenic UMAP [S3]. **f,** Scaled module scoring using gene markers that identify FAP1 (top left), FAP2 (top right), FAP3 (bottom left), and FAP4 (bottom right) clusters from Sarvari *et. al.* superimposed on the fibro-adipogenic UMAP [S4].